Superconductor disks and cylinders in an axial magnetic field. I. Flux penetration and magnetization curves

Ernst Helmut Brandt
Max-Planck-Institut für Metallforschung, D-70506 Stuttgart, Germany
(Received 14 November 1997)

The current density in type-II superconductor circular disks of arbitrary thickness, or cylinders of finite length, in an axial magnetic field is calculated from first principles by treating the superconductor as a conductor with nonlinear resistivity or with linear complex resistivity, both caused by thermally activated depinning of Abrikosov vortices. From these currents follows the magnetic field inside and outside the specimen and the magnetic moment, which in its turn determines the nonlinear and linear ac susceptibilities. The magnetization loops and nonlinear ac susceptibilities are obtained directly by time integration of an integral equation for the current density, which does not require any cutoff or approximation of the magnetic field outside the cylinder. With increasing thickness the results go over from the recently obtained solutions for thin disks in a perpendicular field to the classical behavior of long cylinders in a parallel field. Here this direct method is applied to homogeneous disks with constant thickness, but it applies to any axially symmetric superconductor with arbitrary cross section and inhomogeneity. [S0163-1829(98)06134-7]

I. INTRODUCTION

Material properties of type-II superconductors, like the critical current density and activation energy for thermal depinning, are most conveniently obtained by contact-free magnetic measurements. To achieve high sensitivity the superconductor typically is a thin platelet put into a perpendicular magnetic field. In this perpendicular geometry demagnetization effects are crucial. One may account for these geometry effects by the introduction of a demagnetization factor, but this works only for homogeneously magnetized ellipsoids with linear magnetic response; these three requirements usually are not satisfied in superconductors with vortex pinning. On the other hand, a full three-dimensional (3D) computation of the magnetic response of a superconductor with arbitrary shape is a formidable task which, to my knowledge, has not been tackled so far. As yet it appears even unclear which equations have to be solved when the direction of the currents is not known *a priori* in the full 3D nonlinear problem.

There exist, however, two realistic nonparallel geometries in which the direction of the currents is known, namely, long bars in a perpendicular field where the currents flow along the bar and axial symmetric specimens in an axial field where the currents flow on concentric circles.[1] In both geometries the problem is two dimensional and the current density **J**, vector potential **A**, and electric field **E** are parallel to each other, having only a z or φ component. Recently the theory of a long superconductor bar (or strip, slab) of rectangular cross section in a perpendicular field has been developed in Ref. 1. The present paper extends this method to axial symmetry, in particular to the realistic case of disks or cylinders with arbitrary constant extension along their axis.

The outline of this paper is as follows. In Sec. II explicit expressions are compiled for the current density and magnetization curves of the Bean critical state model for infinitely long cylinders and thin disks in an axial magnetic field. In Sec. III an equation of motion is derived for the current density in cylinders with arbitrary length, which applies to nonmagnetic materials with any nonlinear or linear resistivity and explicitly contains the applied field as a driving force. I then discuss various current-voltage laws and show that in the (rather general) case of a power law, a scaling law relates the frequency and amplitude dependences of the current and field profiles and of the ac susceptibility. Numerical results are presented in Sec. IV in the form of profiles of the current density and magnetic field during penetration and exit of magnetic flux, virgin magnetization curves, hysteresis loops, and current-density profiles. The corresponding nonlinear and linear ac susceptibilities of finite cylinders, which may be used to extract the current-voltage law or the linear complex resistivity from magnetic measurements, are given in part II (Ref. 2).

II. CRITICAL STATE MODEL AND MAGNETIZATION CURVES

A useful model to describe superconductors with strong pinning in high magnetic fields is the critical state model introduced by Bean.[3] This model assumes that the current density $\mathbf{J}(\mathbf{r})$ inside the superconductor is either zero or has the critical magnitude J_c. In regions with $\mathbf{J}=0$, magnetic flux has not penetrated and the magnetic induction is $\mathbf{B}=0$. Regions with $J\equiv|\mathbf{J}|=J_c$ are in the critical state. When the applied field $\mathbf{B}_a=\mu_0\mathbf{H}_a$ is changed, the flux lines (Abrikosov vortices) rearrange themselves such that in regions where J would exceed J_c, J is reduced to J_c again. In general, J_c may depend on the local induction $\mathbf{B}(\mathbf{r})$, and in inhomogeneous materials also explicitly on the position $\mathbf{r}$; J_c may also be anisotropic. In most of this paper $J_c=\text{const}$ is assumed, but the numerical procedures work equally well for any given dependence $J_c(B,\mathbf{r})$; see Sec. IV E.

The orientation of the currents in the critical state model depends on the specimen shape and on the magnetic history, i.e., on the previous applied field $B_a(t)$. For monotonically

increasing $B_a(t)$ the current stream lines in the penetrated region coincide with the virgin flux fronts. In 2D geometry (either very long or very thin prismatic superconductors) the stream lines follow from the simple principle[4] that these curves have a constant distance from the specimen boundary. This general construction principle immediately tells, e.g., that near the convex corners of a polygon-shaped (e.g., rectangular) film in a perpendicular field, and in a rectangular bar in a parallel field, the stream lines are piecewise straight lines performing sharp bends along straight ''discontinuity lines,[5]'' while near the concave edge of an indentation (and near a short crack in the surface) the stream lines form circles centered at the tip of this indentation. These circles meet the regions with straight stream lines along parabolic discontinuity lines. All these topological features are nicely confirmed by magneto-optic observations[5–13] and by direct computations.[14–16] The stream lines may also be visualized by sand piles poured on plates with different shapes.[4]

The long cylinder and thin circular disk in axial field (axis along $\hat{\mathbf{y}}$) are 1D problems. For a *long cylinder* of radius a and length $L=2b$ in a uniform longitudinal applied field H_a the Bean model yields the current density $\mathbf{J}=\hat{\varphi}J(r)$ [$\hat{\varphi}$ is the azimuthal unit vector in the x,z plane, $r=(x^2+z^2)^{1/2}$] and the induction $\mathbf{B}=\hat{\mathbf{y}}B(r)$[$B(r)=\mu_0 H(r)$ if the irreversible magnetization is disregarded],

$$J(r)=\begin{cases} J_c, & r_p\leqslant r\leqslant a, \\ 0, & \text{otherwise}, \end{cases} \tag{1}$$

$$H(r)=\begin{cases} 0, & r\leqslant r_p, \\ H_a-J_c r, & r_p\leqslant r\leqslant a, \\ H_a, & a\leqslant r. \end{cases} \tag{2}$$

Here $r_p=H_a/J_c$ is the radius of the penetrated flux and current front. The magnetic moment of the cylinder of length $L=2b$ in general is $\mathbf{m}=\hat{\mathbf{y}}m$ with

$$m=2\pi\int_0^a dr\ r^2\int_0^b dy\ J(r,y)\ . \tag{3}$$

For long cylinders ($b\gg a$) Eq. (1) yields the virgin magnetic moment

$$m(H_a)=-\pi J_c a^3 L(h-h^2+h^3/3) \tag{4}$$

for $0\leqslant h\leqslant 1$ with $h=H_a/H_p$, where $H_p=J_c a$ is the field of full penetration. For $H_a\geqslant H_p$, i.e., $h\geqslant 1$, m stays constant since the current density has saturated to $J=J_c$ in the entire sample. The initial slope $|m'(0)|$ (the ideal magnetic moment divided by H_a) for a long cylinder is *equal to its volume*,

$$m'(H_a=0)=-\pi a^2 L\ , \tag{5}$$

and the saturated (maximum) magnetic moment is

$$m_{\rm sat}=m(H_a\geqslant H_c)=-\frac{\pi}{3}J_c a^3 L\ . \tag{6}$$

For *thin disks* of radius a and thickness $d=2b\ll a$ in a perpendicular field H_a, the current density averaged over the thickness is $\overline{\mathbf{J}}=\hat{\varphi}\overline{J}(r)$ with[17]

$$\overline{J}(r)=\begin{cases} J_c\dfrac{2}{\pi}\tan^{-1}\dfrac{cr}{(r_p^2-r^2)^{1/2}}, & r\leqslant r_p, \\ J_c, & r_p\leqslant r\leqslant a, \end{cases} \tag{7}$$

where

$$r_p=a/\cosh(H_a/H_c), \tag{8}$$

$$c=(1-r_p^2/a^2)^{1/2}=\tanh(H_a/H_c), \tag{9}$$

$$H_c=J_c b=J_c d/2. \tag{10}$$

For flux-front positions $r_p<a/2$, a good approximation is $\overline{J}(r)=(2J_c/\pi)\arcsin(r/r_p)$. The magnetic moment of the thin disk is

$$m(H_a)=-J_c d a^3\frac{2}{3}\left(\cos^{-1}\frac{1}{\cosh h}+\frac{\sinh|h|}{\cosh^2 h}\right) \tag{11}$$

for $0\leqslant h<\infty$ with $h=H_a/H_c=2H_a/J_c d$. The initial slope $|m'(0)|$ for the thin disk is *much larger than its volume* $\pi a^2 d$,

$$m'(H_a=0)=-8a^3/3\ , \tag{12}$$

and the saturated moment coincides with Eq. (6),

$$m_{\rm sat}=m(H_a\gg H_c)=-\frac{\pi}{3}J_c a^3 d\ . \tag{13}$$

For comparison, the corresponding expressions for a long thin strip of length l and width $2a$ in a perpendicular field are[18]

$$m(H_a)=-J_c d a^2 l\tanh(H_a\pi/J_c d), \tag{14}$$

$$m'(H_a=0)=-\pi a^2 l, \tag{15}$$

$$m_{\rm sat}=m(H_a\gg J_c d\pi)=-J_c d a^2 l. \tag{16}$$

The virgin magnetization curve (11) of the thin Bean disk coincides to better than $0.011m_{\rm sat}$ with that of the long thin strip Eq. (14) if both curves are normalized to unity initial slope $m'(0)$ and unity saturation value $m_{\rm sat}$; cf. Sec. IV C. The normalized Bean magnetization curve of a thin square-shaped disk[13–16] deviates from that of the circular disk by less than $0.002m_{\rm sat}$.[19]

The Bean critical state model of thin strips of constant thickness was first solved for current-carrying strips by Norris.[20] This classical work was then extended to strips in a perpendicular magnetic field without transport current[18] and with transport current,[21,22] and recently to current-carrying strips with an elliptical cross section.[23]

The duality of the strip problems—with applied field or transport current—has no equivalence in the disk problems, since a parallel current cannot be applied without disturbing the symmetry (but adding a radial current is possible, leading to Corbino disk symmetry). However, the problem of a thin ring in a perpendicular field has features of all three prob-

lems, namely, of the disk and the strip with applied field and current; see the recent theories[24,25] and experiments[26,27] on superconducting rings. The extension to superconductors with *finite thickness* so far has been achieved only for a thick strip without transport current in Ref. 1 and for a thick disk in the present paper. Computation of thick strips with transport currents in a perpendicular field is under way.

From the virgin magnetization curves $m(H_a)$ of the Bean model like Eqs. (4) and (11), the complete hysteresis loop in a cycled applied field with amplitude H_0 is obtained by the general prescription[25,28,29]

$$m_\downarrow(H_a,H_0)=m(H_0)-2m\left(\frac{H_0-H_a}{2}\right),$$

$$m_\uparrow(H_a,H_0)=-m(H_0)+2m\left(\frac{H_0+H_a}{2}\right), \qquad (17)$$

where $m_\downarrow$ and $m_\uparrow$ are the branches in decreasing and increasing H_a. If $H_a(t)=H_0\sin\omega t$ is sinusoidal, one may define the ac susceptibility[30]

$$\chi(H_0,\omega)=\frac{i\,\omega}{\pi H_0}\int_0^{2\pi/\omega} m(t)\,e^{-i\omega t}\,dt\,. \qquad (18)$$

In the critical state model χ depends only on the amplitude H_0 but not on the frequency ω. For the thin disk $\chi(H_0)$ was calulated from Eq. (11) in Refs. 29 and 31. The ac susceptibilities of cylinders of various lengths are given in Ref. 2.

III. COMPUTATIONAL METHOD

A. Cylinders of finite length

The aim of this paper is the computation of the magnetic properties of thick circular disks or cylinders of finite length $2b$ and radius a, in a magnetic field $B_a(t)=\mu_0 H_a(t)$ applied parallel to the cylinder axis along y. Here mainly cylinders with constant length $2b$ in a homogeneous applied field will be considered, $r=(x^2+z^2)^{1/2}\leqslant a$, $-b\leqslant y\leqslant b$, but our numerical method applies also to axially symmetric specimens of any cross section and to inhomogeneous $H_a(r,y,t)$.

The material will be characterized by $B=\mu_0 H$, which means zero reversible magnetization or zero lower critical field H_{c1} (practically valid if $|H|\gg H_{c1}$ everywhere), and by a given current-voltage law $\mathbf{E}=E(J)\mathbf{J}/J$ or resistivity $\rho=E/J$. This resistivity may be nonlinear and real, e.g., a power law $E(J)=E_c(J/J_c)^n$, with critical current density $J_c(B)>0$ and exponent $n(B)\geqslant 1$, which in general may both depend on the induction $B(\mathbf{r})$. In the latter example an exponent $n=1$ describes Ohmic behavior and $n\to\infty$ the Bean model. Alternatively, the resistivity $\rho=\rho_{ac}(\omega)$ may be linear, complex, and frequency dependent. By assuming $\mathbf{E}\|\mathbf{J}$ we restrict our considerations here to materials which are isotropic in the xz plane. If required, anisotropic $\mathbf{E(J)}$ laws may also be considered in such computations.[13] However, as shown by Gurevich,[32] some nonlinear anisotropic current-voltage laws (or anisotropic critical current densities) may cause an instability of the current distribution and lead to macroturbulence.

For the short cylinder, to my knowledge exact analytical solutions are not available, neither for the Ohmic limit ($n=1$) nor for the Bean limit ($n\to\infty$). Note that the solution of the London equation for the penetration of magnetic flux is equivalent to the solution of the Ohmic problem, since London superconductors formally exhibit $\rho_{ac}(\omega)=i\omega\mu_0\lambda^2$ where λ is the London penetration depth; cf. Eqs. (20) and (21) and the screening of two coils by a superconducting or Ohmic thin film calculated in Ref. 33.

However, for short cylinders in the Bean limit, one has an explicit expression for the field of full penetration H_p, i.e. the value of the increasing applied field H_a at which the penetrating flux and current fronts have reached the specimen center.[34] At $|H_a|\geqslant H_p$, the current density in the Bean model does not change anymore and the magnetic moment, Eq. (3), saturates to the value $m_{\rm sat}=-(2\pi/3)J_c a^3 b$, Eq. (6). For cylinders with arbitrary aspect ratio b/a, the field of full penetration is[1,34]

$$H_p=J_c b\ln\left[\frac{a}{b}+\left(1+\frac{a^2}{b^2}\right)^{1/2}\right]. \qquad (19)$$

In the limit of a long cylinder ($b\gg a$) this formula yields $H_p=J_c a$ as stated below Eq. (4). For thin disks ($b\ll a$) one obtains, from Eq. (19), $H_p=J_c b\ln(2a/b)$. Inserting this value $H_a=H_p$ into Eq. (8) one finds that the finite thickness $2b$ formally yields an inner cutoff for the thin-film expression (7) at a flux-front position $r_p=a/\cosh[\ln(2a/b)]\approx b$. For comparison, the full penetration field for a long rectangular bar of cross section $2a\times 2b$ in a perpendicular field [Eq. (65) of Ref. 1] has the thin-film limit $H_p=J_c(2b/\pi)\ln(ea/b)$ and yields an inner cutoff of the penetrating flux front at a distance $x_p=a/\cosh(\pi H_a/2J_c b)\to x_p=a/\cosh[\ln(ea/b)]\approx 2b/e$ with $e=2.718$.

B. Equation of motion for the current density

To avoid an explicit computation of the infinitely extended magnetic field $B(\mathbf{r},t)$ outside the cylinder, we try to find an equation of motion for the current density $\mathbf{J}(\mathbf{r},t)$ *inside* the cylinder, using the Maxwell equations $\mathbf{J}=\nabla\times\mathbf{H}$ and $\dot{\mathbf{B}}=-\nabla\times\mathbf{E}$, which imply $\nabla\cdot\mathbf{J}=0$ and $\nabla\cdot\mathbf{B}=0$ if there are no current sources (no contacts) and if $\dot{\mathbf{B}}=0$ at some time t. As usual, the displacement current, which contributes only at very high frequencies, is disregarded in this ''eddy-current approximation.'' As stated in Sec. III A, we describe the superconductor by the material laws $\mathbf{B}=\mu_0\mathbf{H}$ and $\mathbf{E}=E(J)\mathbf{J}/J$.

The main problem is now to find for this geometry an equation for $\mathbf{J}(\mathbf{r},t)$ that explicitly contains the applied field $H_a(t)$, which we assume to be homogeneous for simplicity. In other words, we want to incorporate the known boundary conditions for $H(\mathbf{r},t)$ ($H\to H_a$ for $|\mathbf{r}|\to\infty$) into an equation for $J(\mathbf{r},t)$ which applies only *inside* the specimen. The corresponding problem for parallel geometry (infinite cylinder) is trivial, amounting to the solution of a differential equation for $H(\mathbf{r},t)$ with the boundary condition $H=H_a$ at the surface and in infinite outer space. But for perpendicular geometry the stray field outside the specimen is inhomogeneous and would have to be computed in the entire outer space or approximately in some finite volume extending far beyond the specimen, using some artificial boundary condition at the surface of this large volume.

The desired integral equations for the current density in a perpendicular field recently were found for thin strips[35] and disks,[36] for thin rectangles,[14] and for long bars.[1] Here we derive such an equation for problems with axial symmetry. In this case the current density $\mathbf{J}$, electric field $\mathbf{E}$, and vector potential $\mathbf{A}$ (defined by $\nabla\times A=\mathbf{B}$, $\nabla\cdot\mathbf{A}=0$, $\langle\mathbf{A}\rangle_{\mathbf{r}}=0$) have only *one* component pointing along the azimuthal direction $\hat{\varphi}$; thus $\mathbf{J}=J(r,y)\hat{\varphi}$, $\mathbf{E}=E(r,y)\hat{\varphi}$, and $\mathbf{A}=A(r,y)\hat{\varphi}$. The vector potential of the applied field $\mathbf{B}_a=B_a\hat{\mathbf{y}}$ is $A_a=-(r/2)B_a$. Since $\mathbf{B}=\mu_0\mathbf{H}$, one has $\mu_0\mathbf{J}=-\nabla^2(\mathbf{A}-\mathbf{A}_a)$, or explicitly in axial symmetry, $\mu_0 J=-\nabla^2[A+(r/2)B_a]$. The solution of this Laplace equation in cylindrical geometry is

$$A(\mathbf{r})=-\mu_0\int_0^a dr'\int_0^b dy'\ Q_{\rm cyl}(\mathbf{r},\mathbf{r}')\ J(\mathbf{r}')-\frac{r}{2}B_a, \tag{20}$$

with $\mathbf{r}=(r,y)$ and $\mathbf{r}'=(r',y')$. The integral kernel

$$Q_{\rm cyl}(\mathbf{r},\mathbf{r}')=f(r,r',y-y')+f(r,r',y+y'), \tag{21}$$

with

$$f(r,r',\eta)=\int_0^{\pi}\frac{d\varphi}{2\pi}\,\frac{-r'\cos\varphi}{(\eta^2+r^2+r'^2-2rr'\cos\varphi)^{1/2}}, \tag{22}$$

is obtained by integrating the 3D Green function of the Laplace equation, $1/(4\pi|\mathbf{r}_3-\mathbf{r}'_3|)$ with $\mathbf{r}_3=(x,y,z)$, over the angle $\varphi=\arctan(z/x)$. The function $f(r,r',\eta)$ may be expressed in terms of elliptic integrals, but here it is more convenient to evaluate the φ integral (22) numerically. A high-precision integration method which accounts for the infinities of the periodic integrand $g(\varphi)$ in Eq. (22) at $\varphi=0,\ 2\pi,\ \ldots,$ etc., uses the substitution $\varphi=\varphi(u)=\pi u-\sin\pi u (u=0,\ldots,1)$ and weight function $\varphi'(u)=\pi-\pi\cos\pi u$ with equidistant grid $u_i=(i-\frac{1}{2})/M$, $(i=1,2,\ldots,M,\ M\approx 30)$ by writing Eq. (22) in the form

$$f=\int_0^{\pi} g(\varphi)\ d\varphi=\int_0^1 g[\varphi(u)]\ \varphi'(u)\ du$$
$$\approx\frac{1}{M}\sum_{i=1}^{M} g[\varphi(u_i)]\varphi'(u_i). \tag{23}$$

To obtain the desired equation for $J(r,y,t)$ we express the induction law $\nabla\times\mathbf{E}=-\dot{\mathbf{B}}=-\nabla\times\dot{\mathbf{A}}$ in the form $E=-\dot{A}$. The gauge of $\mathbf{A}$, to which an arbitrary curl-free vector field may be added, presents no problem in this simple geometry. Knowing the material law $E=E(J)$, e.g., $E=E_c(J/J_c)^n\mathrm{sgn}(J)$ or a linear and complex $E=\rho J$, one obtains $\dot{A}=-E(J)$. This relation between $\dot{A}$ and J allows us to eliminate either A or J from Eq. (20). Eliminating A, one obtains

$$E[J(\mathbf{r},\mathbf{t})]=\mu_0\int_S d^2r'\,Q_{\rm cyl}(\mathbf{r},\mathbf{r}')\dot{J}(\mathbf{r}',t)+\frac{r}{2}\dot{B}_a(t). \tag{24}$$

This implicit equation for the current density $J(\mathbf{r},t)$ contains the time derivative $\dot{J}$ under the integral sign. It may be used in this form (containing the kernel $Q_{\rm cyl}$ rather than the reciprocal kernel $Q_{\rm cyl}^{-1}$) when one is interested in the linear response to a periodic signal, $\dot{B}_a\propto i\omega\exp(i\omega t)$. In this case the time dependence of $\dot{J}(\mathbf{r},t)=J(\mathbf{r})\exp(i\omega t)$ is explicitly known and the amplitude $J(\mathbf{r})$ follows from a *linear* integral equation as described in Ref. 2. In the general case of nonlinear $E(J)$ and arbitrary sweep of $B_a(t)$, the time integration of Eq. (24) has to be performed numerically as described in Ref. 1. For this purpose, the time derivative should be moved out from the integral to obtain $\dot{J}$ as an explicit functional of J and $\dot{B}_a$. This inversion may be achieved by tabulating the kernel $Q_{\rm cyl}(\mathbf{r},\mathbf{r}')$ on a 2D grid $\mathbf{r}_i$, $\mathbf{r}_j$ and then inverting the matrix Q_{ij} to obtain Q_{ij}^{-1}, which is the tabulated reciprocal kernel $Q_{\rm cyl}^{-1}(\mathbf{r}_i,\mathbf{r}_j)$. The equation of motion for the azimuthal current density $J(r,y,t)$ then reads

$$\dot{J}(\mathbf{r},t)=\mu_0^{-1}\int_0^a dr'\int_0^b dy'\ Q_{\rm cyl}^{-1}(\mathbf{r},\mathbf{r}')\left[E(J)-\frac{r'}{2}\dot{B}_a\right]. \tag{25}$$

This nonlocal and (in general) nonlinear diffusion equation for $J(r,y,t)\hat{\varphi}$ looks very similar to the corresponding equation for the longitudinal current density $J(x,y,t)\hat{\mathbf{z}}$ in strips, bars, or slabs derived in Ref. 1. The same numerical program can thus be used to compute the electrodynamics of long bars in a perpendicular field and of an axially symmetric specimens in axial field.

As they stand, Eqs. (20) and (24) apply to cylinders with constant height $2b$ or disks with constant thickness. But they are easily generalized to an arbitrary cross section of an axially symmetric specimen by replacing the integration boundary b for y by a function $b(r)$ of the radius $r=(x^2+z^2)^{1/2}$. For example, $b(r)=(a^2-r^2)^{1/2}$ describes a sphere and $b(r)=b(0)(1-r^2/a^2)^{1/2}$ an axially symmetric ellipsoid.

One may also drop the mirror symmetry at the plane $y=0$, expressed by Eq. (21). This allows us to consider, e.g., superconductors of conical shape in an inhomogeneous applied field $H_a(r,y,t)$. In this case one replaces in Eq. (25) the applied vector potential $\mathbf{A}_a=(r/2)B_a(t)\hat{\varphi}$ by some other axially symmetric vector potential $A(r,y,t)\hat{\varphi}$, which is caused, e.g., by a small coil or by a permanent magnet which levitates the superconductor. Our method thus allows us to compute repulsive or attractive hysteretic levitation forces on magnets and superconductors in axial symmetric configurations.

C. Interpretation of the equation of motion

The equation (25) for $\dot{J}(\mathbf{r},t)$ as a function of $J(\mathbf{r},t)$ and of $\dot{B}_a(t)$ ''works,'' i.e., the solution $J(\mathbf{r},t)$ is obtained by direct numerical time integration, starting, e.g., with $B_a=0$ and $J=0$ at time $t=0$, and then increasing B_a gradually to obtain a nontrivial solution $J(\mathbf{r},t)$. But how is the boundary condition $B(r\to\infty)\to B_a$ actually incorporated into Eq. (25) ?

To answer this question one has to reconsider the derivation of Eq. (25). One realizes that in the equation $\mu_0\mathbf{J}=-\nabla^2(\mathbf{A}-\mathbf{A}_a)$ above Eq. (20) the last term actually could have been omitted because inside the specimen one has $\nabla^2\mathbf{A}_a=0$ or, explicitly, $\nabla^2(r/2)B_a=0$, since the currents

causing the applied field flow in a faraway coil. But this omission would have left us without the B_a terms in Eqs. (20) and (25). While in Eq. (20) the term $(-r/2)B_a$ should be clearly there, the meaning of the term $(-r/2)\dot{B}_a$ in Eq. (25) is less trivial. One may argue that, since the operator $Q(\mathbf{r},\mathbf{r}')$ is the inverse of the Laplacian operator ∇^2, the inverted kernel $Q^{-1}(\mathbf{r},\mathbf{r}')$ should be identical to ∇^2 and therefore the last term in Eq. (24) should vanish. This is indeed true for positions $\mathbf{r}$ *inside* the specimen: One can show that $\int d^2r'\ Q_{\rm cyl}^{-1}(\mathbf{r},\mathbf{r}')r'=0$ for $\mathbf{r}$ inside the cylinder. But for $\mathbf{r}$ on the cylinder *surface*, this term is infinite and describes a screening current flowing in a thin surface layer.

The existence and size of this surface screening current is easily seen when one starts at time $t=0$ with $B_a=0$ and $J=0$ and then switches on the applied field such that $\dot{B}_a\neq 0$ in Eq. (25). Immediately after that, at time $t=+\epsilon$, the induction and current density inside the cylinder are still zero since they need some time to diffuse into the conducting material. Therefore, at $t=+\epsilon$ also the electric field $E(J)$ is zero and thus the first term in Eq. (25) vanishes. What remains is the last term, which should be the time derivative of the Meissner screening current $J_{\rm scr}$. This surface screening current is thus

$$J_{\rm scr}(\mathbf{r},t)=-H_a(t)\int_0^a dr'\int_0^b dy'\ Q_{\rm cyl}^{-1}(\mathbf{r},\mathbf{r}')\ \frac{r'}{2}\,. \quad (26)$$

The thickness of this current-carrying layer depends on the choice of the computational grid in the cylinder. The layer thickness may be reduced, and the precision of the computed magnetic moment enhanced, by chosing a nonequidistant grid which is denser near the cylinder surface. If each grid point $\mathbf{r}_i$ has a weigth w_i such that with integrands $g(\mathbf{r})$ typical for cylindrical problems the integrals are well approximated by sums of the form

$$\int\ g(\mathbf{r})\ d^2r\approx\sum_i\ g(\mathbf{r_i})w_i\,, \quad (27)$$

then the matrix which has to be inverted is the original matrix times this weight. Namely, for arbitrary functions $g(\mathbf{r})$ and $h(\mathbf{r})$ tabulated inside the cylinder as $g_i=g(\mathbf{r}_i)$ and $h_i=h(\mathbf{r}_i)$, one has with the definition

$$h(\mathbf{r})\equiv\int d^2r\ Q(\mathbf{r},\mathbf{r}')g(\mathbf{r}), \quad (28)$$

$$h_i\approx\sum_j\ Q_{ij}w_j\ g_j\,,\quad g_i\approx\sum_j\ (Q_{ij}w_j)^{-1}h_j\,. \quad (29)$$

Thus the required reciprocal matrix is the inverse of $Q_{ij}w_j$ (no summation over j in this product). An appropriate choice of such a nonequidistant grid $\mathbf{r}_i=(r_i,y_i)$ is obtained, e.g., by the substitutions $r=r(u)=\frac{1}{2}(3u-u^3)a$, $y=y(v)=\frac{1}{2}(3v-v^3)b$, and then tabulating $u=0,\ldots,1$ and $v=0,\ldots,1$ on equidistant grids $u_k=(k-\frac{1}{2})/N_r(k=1,\ldots,N_r)$ and $v_l=(l-\frac{1}{2})/N_y(l=1,\ldots,N_y)$, yielding a 2D grid of $N=N_r\cdot N_y$ points with weights vanishing at the boundaries $r=a$ and $y=b$, namely, $w_i=w_rw_y$ with $w_r=dr_k/dk=\frac{3}{2}(1-u_k^2)a/N_r$ and $w_y=dy_l/dl=\frac{3}{2}(1-v_l^2)b/N_y$.

D. Current-voltage laws

The equations of motion (24) and (25) still apply to any current-voltage law $E(J)$. From the theories of collective creep[37,38] and also from the vortex glass picture[39] one obtains the useful interpolation formula[40]

$$E(J)=E_c\exp\left(-\frac{U(J)}{kT}\right),$$

$$U(J)=U_0\frac{(J_c/J)^\alpha-1}{\alpha}. \quad (30)$$

Here $U(J)$ is a current-dependent activation energy for depinning which vanishes at the critical current density J_c, and α is a small positive exponent. Formally, for $\alpha=-1$ expression Eq. (30) coincides with the result of the Kim-Anderson model,[40] $E(J)=E_c\exp[(U_0/kT)(1-J/J_c)]$. For $\alpha=1$ one gets $E(J)=E_c\exp[(U_0/kT)(J_c/J-1)]$. In the limit $\alpha\to 0$ one has $U(J)=U_0\ln(J_c/J)$ and thus

$$E(J)=E_c(J/J_c)^n\quad\text{with}\quad n=U_0/kT\,. \quad (31)$$

This power law has been found in many experiments. It contains only one essential parameter, the exponent n, besides the trivial prefactor E_c/J_c^n. For $n=1$ it describes an Ohmic conductor with constant resistivity $\rho=E/J$, which applies also to superconductors in the regime of thermally activated flux flow[41] (TAFF) at low frequencies. In the limit $n\to\infty$ the power law (31) is equivalent to the Bean model, and for $1\ll n<\infty$ it describes flux creep. In general, the prefactor E_c and activation energy U in Eq. (30) depend on the local induction $B(\mathbf{r})$; therefore, in general also $n(B,T)$ and $J_c(B,T)$ depend on B. But this B dependence may be disregarded if B is sufficiently large. In the following computations I shall use the simple power law (31) to model superconductors with flux creep.

E. Useful scaling law

For the power law current-voltage curve (31), $E\propto J^n$ or $\rho=E/J\propto J^\sigma$ with $\sigma=n-1$, a general scaling law follows from the Maxwell equations when $\mathbf{B}=\mu_0\mathbf{H}$.[25] Namely, when one changes the time unit by an arbitrary constant factor of c and the current and field units by a factor of $c^{1/\sigma}$ where $\sigma=n-1$, then Eqs. (24) and (25) for the current density are invariant; i.e., the same solutions result for the scaled quantities. This means, if these equations and the Biot-Savart law (20) are expressed in terms of a new time $\tilde{t}=t/c$, then the new solutions take the form

$$\tilde{J}(\mathbf{r},\tilde{t})=J(\mathbf{r},t)c^{1/\sigma},\quad \tilde{B}_a(\tilde{t})=B_a(t)c^{1/\sigma},$$

$$\tilde{\mathbf{B}}(\mathbf{r},\tilde{t})=\mathbf{B}(\mathbf{r},t)c^{1/\sigma},\quad \tilde{m}(\tilde{t})=m(t)c^{1/\sigma}. \quad (32)$$

In particular, when $B_a(t)=B_0\sin\omega t$ is periodic, the shape of the hysteretic magnetization curve $m(B_a)$ remains *unchanged* if one increases ω by a factor of c and B_0 by a factor of $c^{1/\sigma}$. By the same token, the complex susceptibility $\chi(B_0,\omega)$ normalized to $\chi(0,\omega)=\chi(B_0,\infty)=-1$, i.e., to the ideal diamagnetic limit occurring at zero amplitude or infinite frequency, remains unchanged during such scaling.

A useful consequence of this scaling law is thus that the normalized ac susceptibility $\chi(B_0,\omega)$ and the shape of the hysteresis loop $m(B_a)$ depend only on the combinations $B_0/\omega^{1/\sigma}$ or ω/B_0^{σ}. One may write, e.g.,

$$\chi(B_0,\omega)=f_\sigma[\beta B_0/\omega^{1/\sigma}+\omega/(\beta B_0)^\sigma], \tag{33}$$

where $f_\sigma(x)$ is a universal complex function (depending on σ and on the geometry) and β is an arbitrary constant of the same dimension as $\omega^{1/\sigma}/B_0$, introduced to make the argument x of $f_\sigma(x)$ dimensionless. Therefore, if $\chi(B_0,\omega)$ is known for a wide range of amplitudes B_0 at one frequency $\omega/2\pi$, then the scaling relation (33) gives us χ for different frequencies. A further consequence is that the polar plots[25,27,42] $\chi''(\chi')$ of the complex ac susceptibility $\chi=\chi'-i\chi''$ depend only on the exponent σ. Though this scaling law was derived for a power law $E\propto J^n$, it applies to a wide class of nonlinear $E(J)$ if one defines $\sigma=n-1=\partial(\ln E)/\partial(\ln J)-1$ taken at $J\approx J_c$, i.e., at the characteristic current density of the experiment. With this definition $E(J)$, Eq. (29), yields $n=(U_0/kT)(J_c/J)^\alpha\approx U_0/kT$.

The scaling relation (33) correctly yields the two limiting cases of Ohmic conductors, which exhibit $\sigma=0$ and $\chi=\chi(\omega)$, and of Bean superconductors, exhibiting $\sigma\to\infty$ and $\chi=\chi(B_0)$. It thus connects these two limits in a natural way.

IV. RESULTS

A. Flux penetration and exit

The time integration of Eq. (25) is described in Ref. 1. To obtain flux fronts and magnetic field lines, an equidistant spatial grid $\mathbf{r}_i$ works well, but for accurate computation of magnetization curves and susceptibilities a nonequidistant grid with denser points near the cylinder surfaces is preferred. First one tabulates the matrix $Q_{ij}=Q(\mathbf{r}_i,\mathbf{r}_j)$, Eq. (21). As with the strip geometry, the diagonal terms of Q_{ij} formally diverge as $\ln|\mathbf{r}_i-\mathbf{r}_j|$ and have to be cut off appropriately. The optimal choice of the terms Q_{ii} in the strip and cylinder geometries is not yet solved satisfactorily; cf. the Appendix. Good numerical accuracy is achieved by replacing η^2 by $\eta^2+\epsilon^2$ in Eq. (22) with $\epsilon^2=0.015\,dx\,dy$ where $dx=a/N_x$ and $dy=b/N_y$ are the grid spacings. (To stress the similarity with the bar geometry we write here N_x for N_r and dx for dr.) This ϵ value works well when the grid cells are approximately quadratic, $dx\approx dy$ or $N_y\approx N_x b/a$. To check the accuracy one may use the fact that for $n\gg 1$ the profiles of the penetrating magnetic field should be positive outside the flux-free core, go steeply to zero at the core boundary, and stay zero inside the core; cf. Figs. 9 and 10 below. If ϵ is chosen too large or too small, then B just inside the flux front artificially may take a small negative or positive value. In principle, some method of finite elements might be used to define the matrix Q_{ij} and obtain finite diagonal elements,[4] but so far our trials gave less accurate results than the above definition of Q_{ij}; see also Sec. IV E. This matrix is then inverted to yield Q_{ij}^{-1}. Here we use units $a=J_c=E_c=\mu_0=1$, yielding $E=J^n$, Eq. (31). Finally, time integration of Eq. (25) is performed by writing the continuous current density as a discrete vector $J(r_i,y_i,t)=J_i(t)$ and its equation of motion (25) as a matrix equation,

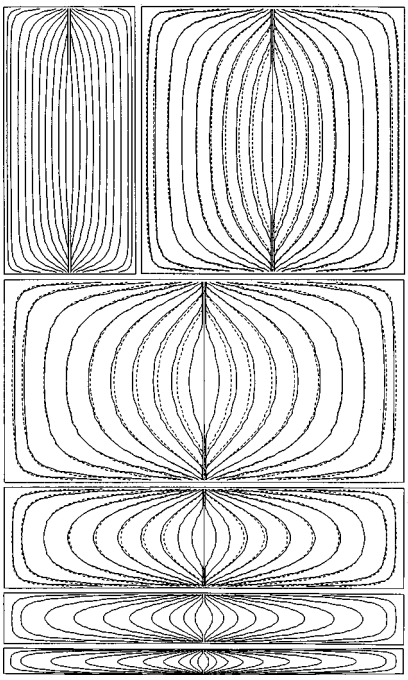

FIG. 1. Current and flux fronts in superconductor cylinders with aspect ratios $b/a=2$, 1, 0.5, 0.25, 0.125, and 0.0625 in an axial magnetic field H_a. First H_a is increased gradually from zero to $0.9H_p$ (solid lines; shown are $H_a/H_p=0.05$, 0.1, 0.2, . . . ,0.9) and then decreased again (dashed lines; $H_a/H_p=0.8$, 0.7, 0.5, 0.3, . . . , -0.5, -0.7), where H_p is the field of full penetration, Eq. (19). Shown is the Bean limit ($n=51$) at a constant ramp rate $|\dot B_a|=E_c/a$. For increasing H_a the depicted contour lines $J=\pm J_c/2$ separate the inner core with $J=0$ from the outer regions with $J=\pm J_c$. For decreasing H_a the contour lines $J=0$ separate regions with $+J_c$ and $-J_c$. In the genuine Bean limit ($n\to\infty$) the solid and the dashed lines should exactly coincide.

$$\dot J_i(t)=\frac{b}{N}\sum_j\, Q_{ij}^{-1}\left[J_j(t)^n-\frac{r_j}{2}\dot B_a(t)\right]; \tag{34}$$

cf. Eq. (20) of Ref. 1. The time integration of this first-order nonlinear differential matrix equation for $J_i(t)$ may be performed by starting at time $t=0$ with $J_i(0)=0$ and then increasing t in steps dt to obtain $J_i(t+dt)=J_i(t)+\dot J_i(t)dt$. The computational speed and stability of this time integration are strongly increased by using a variable time step $dt=c_1/(\max|\rho|+0.01)$ with $\rho=E/J$ and $c_1=0.3/(N_x^2 n)$ in units of $a=J_c=E_c=\mu_0=1$. Up to grid sizes of about $N=N_xN_y\approx 1200$ this calculation may be performed easily on a PC.

The shapes of the penetrating flux fronts for finite cylinders of various lengths in increasing axial field B_a are shown in Fig. 1 for $n=51$. These fronts look very similar to the fronts in long rectangular bars with the same aspect ratio b/a shown in Fig. 2 of Ref. 1. We compute these fronts most conveniently as the two contour lines where the current density J equals $\pm\frac{1}{2}J_c$. Other methods for obtaining these fronts within the Bean model are given in Refs. 3 and 43–46.

The dashed lines in Fig. 1 are the flux fronts which form when B_a is *decreased* again after an almost complete penetration of flux. At these penetrating fronts of flux with opposite sign, J jumps from $-J_c$ to $+J_c$; the depicted dashed

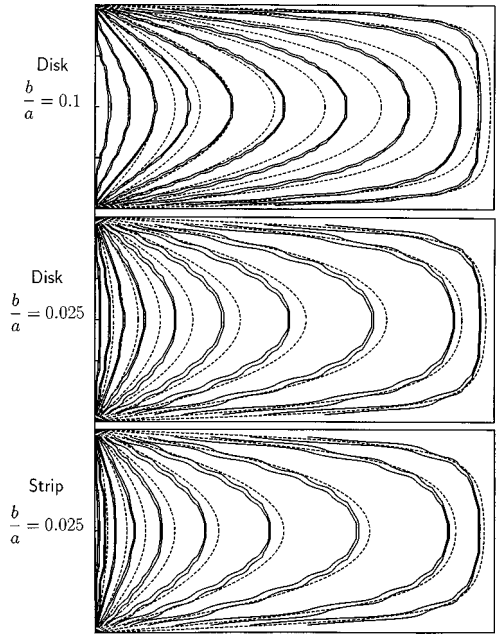

FIG. 2. Comparison of the computed flux fronts (solid lines) with the analytic expression (34) (dashed lines) for disks with $b/a=0.1,\ 0.025$, and for strips with $b/a=0.025$ (from top to bottom). Shown are the contour lines $J=J_c/2$ in half the cross section in increasing applied field $H_a/H_p=0.5,\ 0.1,\ 0.2,\ \ldots,0.9$. For clarity the thickness $2b$ is exaggerated in these plots by factors of 2.5 and 10. The creep exponent is $n=51$ and the number of grid points, $N_r\times N_y=80\times 14$ and 90×7.

lines are thus chosen as the contours $J=0$. In the genuine Bean model ($n\to\infty$) these fronts should have the same shape as the incoming virgin fronts. In Fig. 1 the fronts are plotted for $H_a/H_p=0,\ 0.05,\ 0.1,\ 0.2,\ \ldots,0.9,\ 0.8,\ 0.7,\ 0.5,\ 0.3,\ \ldots,-0.5,-0.7$, where H_p is given by Eq. (19). These intervals are twice as large during the decrease of H_a than during the increase. Therefore, the two series of fronts should exactly coincide within the Bean model; see also Eq. (17). For the depicted large creep exponent $n=51$ the solid and dashed flux fronts indeed coincide almost perfectly. Finite creep ($n<\infty$) initially leads to a slower penetration of oppositely oriented flux, but then these new flux fronts overtake the virgin fronts and reach the specimen center before H_a is decreased to $-H_p$.

The similarity of the Bean flux fronts for not too thick disks and strips ($b\ll a$) follows from the similarity of the solutions for the thickness-averaged current density $\overline{J}$ of thin disks and strips in a perpendicular field; cf. Eq. (7) for the disk. The same equation (7) applies also for the long strip if r is replaced by x and $H_c=bJ_c$ by $H_c=2bJ_c/\pi$. Since inside the disk $|J|$ is either 0 or J_c, the shape of the flux fronts in thin disks follows from $\overline{J}(r)$, Eq. (7), as

$$y(r)=\pm b\left[1-\frac{\overline{J}(r)}{J_c}\right]\approx b\,\frac{2}{\pi}\arccos\frac{r}{r_p} \tag{35}$$

for $r\leqslant r_p$. Figure 2 compares the computed flux fronts with Eq. (35) for a disk with aspect ratio $b/a=0.1$ and for disks and strips with $b/a=0.025$ and creep exponent $n=50$. For thin disks and strips the qualitative agreement is good as

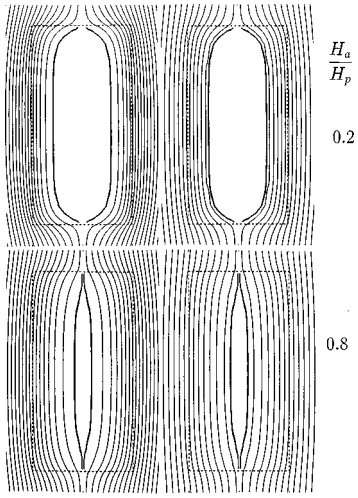

FIG. 3. The magnetic field lines during flux penetration into a cylinder with $b/a=2$ and creep exponent $n=51$ at applied field values $H_a/H_p=0.2$ (top) and 0.8 (bottom). Left: contours of the vector potential $A(r,y)$ at equidistant levels. Right: contours of $rA(r,y)$ at nonequidistant levels; see text. The rectangular frame indicates the border of the disk and the bold lines (the contours $J=\pm J_c/2$) delimit the field- and current-free core.

long as the penetration radius r_p, Eq. (8), exceeds the disk thickness $2b$. At larger applied fields, when $r_p<b$, the computed flux front detaches from the surface of the disk, and the field- and current-free core becomes isolated from the outer world. From Eq. (19) one finds that for $b\ll a$ full penetration occurs when r_p, Eq. (8), has reached the value $(2/e)b=0.74b$.

In specimens with finite thickness the computed flux fronts penetrate faster than predicted by Eq. (34); i.e., at a given value of H_a the real front has penetrated deeper than the thin-limit front (34). This effect becomes larger when a smaller exponent n is used. For disks and strips with $b/a=0.025$ and $n=51$ the depicted fronts are nearly identical except near the specimen center. The wiggles in the plotted fronts (computed as the contours $J=J_c/2$) are due to the small number of grid planes, $N_y=7$, in the grid used of $N=N_x\times N_y=80\times 7$ points.

B. Local magnetic field

The magnetic field lines in increasing axial field $H_a(t)$ are shown in Figs. 3–6 for cylinders with various aspect ratios $b/a=2$ (long cylinder, 12×24 grid points), $b/a=0.5$ (short cylinder, 24×12 grid), $b/a=0.25$ (thick disk, 28×7 grid), and $b/a=0.1$ (thin disk, 60×6 grid), for creep exponent $n=51$. These magnetic field lines, and also the contour lines and profiles of the electric field not shown here, look similar for cylinders and bars with same cross section $2a\times 2b$; see Refs. 1 and 47. However, a general difficulty arises when one tries to visualize 3D magnetic field lines with axial symmetry in a 2D plot. While for infinite strips or bars the field lines of $\mathbf{B}(x,y)=\nabla\times\hat{\mathbf{z}}A(x,y)$ are actually 2D and coincide with the contour lines of the vector potential $A(x,y)$ directed along the strip, this elegant plotting method does not work for a cylinder in an axial field. Namely, for a bar one has $B_x=\partial A/\partial y$ and $B_y=-\partial A/\partial x$, but for a cylinder with $\mathbf{A}$

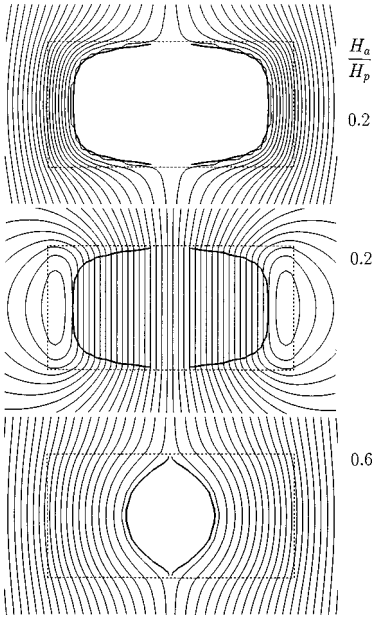

FIG. 4. Magnetic field lines during flux penetration into a short cylinder with $b/a=0.5$ and creep exponent $n=51$ at applied field values $H_a/H_p=0.2$ (top, middle) and $H_a/H_p=0.6$ (bottom). The middle part shows the current-caused field $B-B_a$. Depicted are the contours of $rA(r,y)$ at nonequidistant levels. The bold lines are the contours $J=\pm J_c/2$.

along $\varphi=\mathrm{atan}(z/x)$ the components of $\mathbf{B}(r,y)=\nabla\times[\hat{\varphi}A(r,y)]$ are $B_r(r,y)=\partial A/\partial y$ and $B_y=-(1/r)(\partial/\partial r)\times(rA)$.

For the present problem, reasonable magnetic field lines are obtained by plotting contour lines of $rA(r,y)$ at nonequidistant levels $rA=\mathrm{const}\times(\mu-\frac{1}{2})|\mu-\frac{1}{2}|$ with $\mu=0,\pm1,\pm2,\ldots$. These lines are directed along $\mathbf{B}$ and they are equidistant when $\mathbf{B}=\mathrm{const}$, with (2D) line density proportional to the (3D) field strength B. But at positions where A goes to zero away from the axis $r=0$, the density of these

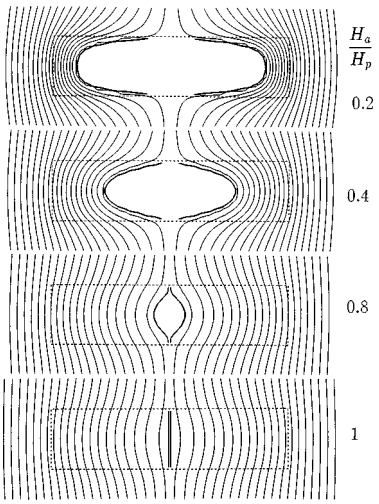

FIG. 5. Magnetic field lines during flux penetration into a thick disk with $b/a=0.25$ and creep exponent $n=51$ at $H_a/H_p=0.2,\ 0.4,\ 0.8$, and 1 (from top to bottom). Depicted are the contours of $rA(r,y)$ at nonequidistant levels. The bold lines are the contours $J=\pm J_c/2$.

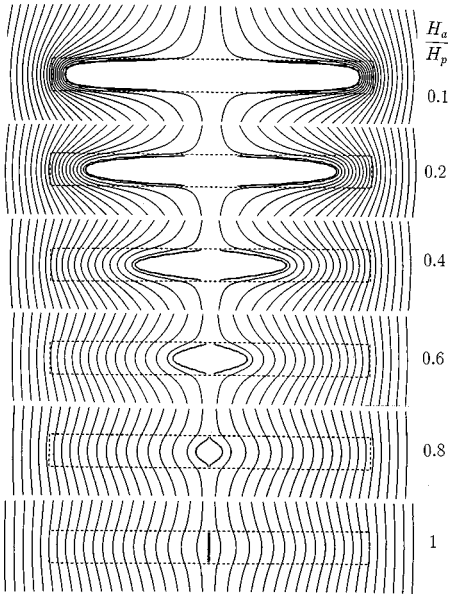

FIG. 6. Magnetic field lines during flux penetration into a thin disk with $b/a=0.1$ and creep exponent $n=51$ at $H_a/H_p=0.1,\ 0.2,\ 0.4,\ 0.6,\ 0.8$, and 1 (from top to bottom). Depicted are the contours of $rA(r,y)$ at nonequidistant levels. The bold lines are the contours $J=\pm J_c/2$.

contour lines exaggerates the real field strength B. This can be seen in Fig. 3, where the field lines are plotted by both methods. In this case ($b/a=2$) the axial component $B_y(r,y)$ in the middle plane $y=0$ goes linearly to zero at the flux front; cf. Fig. 9 below.

In Fig. 3 (left column) and Figs. 4–6 the field lines are plotted as the contour lines $rA=\pm\mathrm{const}\times(1,3,5,\ldots)$; see above. These figures show the field lines of the *total* magnetic field $\mathbf{B}(r,y)$ in increasing external field B_a. The middle part of Fig. 4 shows also the field $\mathbf{B}(r,y)-\hat{\mathbf{y}}B_a$ caused by the currents circulating in the cylinder. Inside the current-free core this field is exactly homogeneous and opposed to the applied field B_a; the superconducting cylinder behaves thus like an ideal coil with constant current density in an optimally shaped cross section.

Figure 7 shows the magnetic field lines when H_a is decreased again after full penetration of flux and current has been reached at $H_a=H_p$, Eq. (19). In this figure the field lines are plotted as the contour lines of A, which in the depicted volume close to the superconductor give virtually identical pictures for strips and disks with the same aspect ratio b/a. Shown are the field values (from top) $H_a/H_p=0.5,\ 0.25,\ 0,\ -0.25,\ -0.5$, and -0.75. Note that the picture of the field lines changes qualitatively several times when H_a is decreased from H_p to $-H_p$. In particular, at $H_a/H_p=-0.25$ the field strength B has two zeros away from the disk on the axis. Near these zeros the magnetic field is quadrupolar. In such free minima of $B^2(x,y,z)$ a superconductor,[48] and in principle any diamagnet,[49,50] can levitate freely. Note also that along any diameter the current density changes its direction three times: from $-J_c$ to $+J_c$ at the flux front, to $-J_c$ at the center, and again to $+J_c$. Therefore, in Fig. 7 the also depicted contour lines $J=0$ mark the lens-shaped core into which the opposite flux has not yet penetrated, and they mark the specimen center.

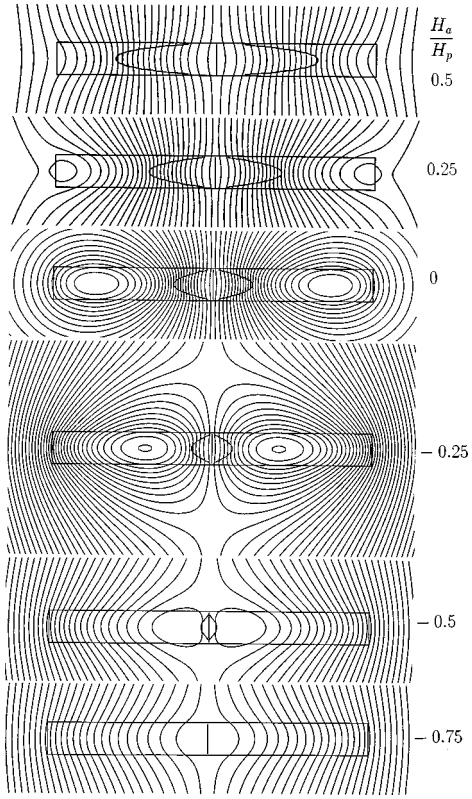

FIG. 7. Magnetic field lines during the penetration of flux of opposite orientation, occurring when H_a is decreased again after it had first been increased to the field of full penetration H_p, Eq. (19). Shown are the field lines (the contour lines of A) for a strip with $b/a=0.1$ and creep exponent $n=51$ at $H_a/H_p=0.5$, 0.25, 0, -0.25, -0.5, and -0.75 (from top to bottom). Also indicated are the specimen cross section and the lens-shaped core into which the opposite flux has not yet penetrated.

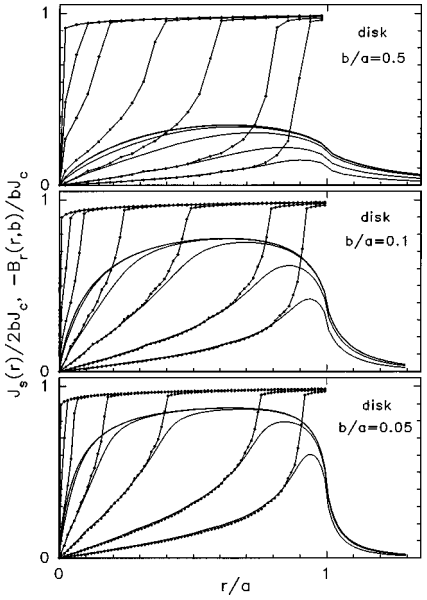

FIG. 8. The thickness-integrated sheet current $J_s(r)$ for disks with $b/a=0.5$, 0.1, and 0.05 and creep exponent $n=51$ during flux penetration, plotted in units $J_c a$ for applied fields $H_a/H_p=0.1$, 0.2, 0.4, 0.6, 0.8, 0.9, and 1 (from right to left, the solid line with dots). The bold lines give the radial (tangential) component of the magnetic field at the surface, $B_r(r,b)$, which for thin disks with $b \ll a$ should coincide with the depicted curves $J_s/2$ for $r<a$ and vanish for $r>a$ (outside the disk). The finite thickness $2b$ rounds the jumps of $B_r(r)$ at the flux front and at the edge.

Figure 8 shows the tangential component $B_r(r,y)$ of the magnetic field at the flat surface $y=b$ of cylinders with $b/a=0.5$, 0.1, and 0.05 in an axial field H_a. This radial component is compared with the current density integrated over the thickness, the sheet current $J_s(r)=2b\overline{J}$. In the thin-film limit, $B_r(r,b)$ should coincide with $J_s(r)/2$. This coincidence is nicely seen near the center. At the flux front the computed $J_s(r)$ (for exponent $n=51$) has a sharp bend, and for thin disks $J_s(r)$ is well described by Eq. (7). For the depicted thicknesses, $B_r(r,d)$ is still rounded at the front and near the edge of the cylinder, since B_r is caused by currents flowing not only in a shell of constant radius r. But in the thin-film limit $b \ll a$, $B_r(r,y)$ is generated mainly by currents flowing in the immediate vicinity of r.

Figures 9 and 10 show the axial magnetic field $B_y(r,y)$ at the flat surfaces $y=\pm b$ and at the central plane $y=0$ for cylinders and disks with various side ratios in an increasing axial field. Note that the field on the middle plane $y=0$ has a nearly constant slope $|\partial B_y/\partial r| \approx J_c$, down to aspect ratios of $b/a \geq 0.25$, as predicted by the Bean model for long cylinders with $b \gg a$. The field at the surface, which may be measured by magneto-optics, also has a nearly constant slope, but the slope is smaller than J_c. For thin disks with $b/a \leq 0.25$, a sharp cusp in B_y develops at the edge of the disk; this cusp is much sharper in the middle plane than in the surface planes. For very thin disks the computed $B_y(r)$ coincides with the one calculated directly from the sheet current (7). To my knowledge, an analytic expression for this $B_y(r)$ is available only for strips[18] but not for disks.[17,29,31]

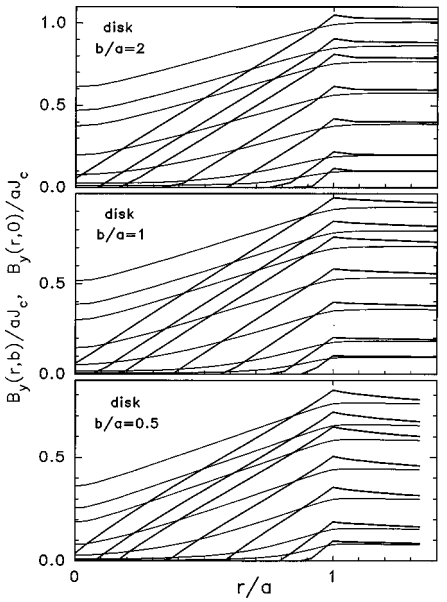

FIG. 9. Profiles of the axial flux density $B_y(r,y)$ at the surface $y=\pm b$ (thin lines) and at the central plane $y=0$ (thick lines). Shown are the results for cylinders with $b/a=2$, 1, and 0.5 in an increasing applied axial field $H_a/H_p=0.1$, 0.2, 0.4, 0.6, 0.8, 0.9, and 1 at $n=51$. The corresponding radial component B_r is plotted in Fig. 8.

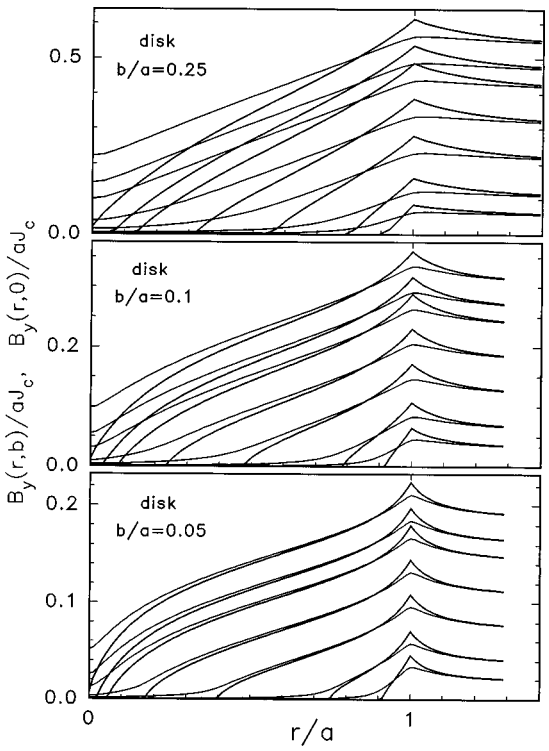

FIG. 10. As in Fig. 9, but for thinner disks with side ratios $b/a=0.25$, 0.1, and 0.05.

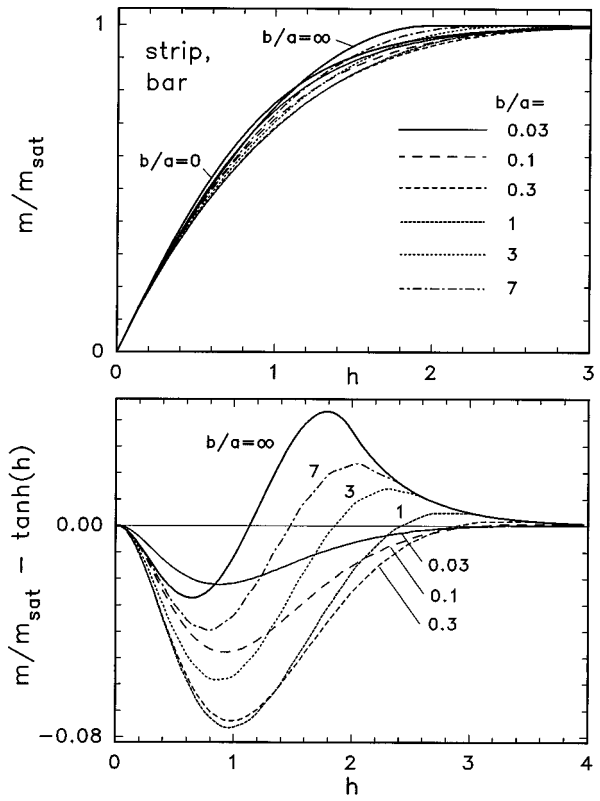

FIG. 11. Top: virgin magnetization curves $m(H_a)$ for strips or bars with side ratios $b/a=0.03$, 0.1, 0.3, 1, 3, and 7 in increasing perpendicular field H_a in the Bean limit ($n=101$). The plots are in reduced units m/m_{sat} vs $h=H_a m'(0)/m_{sat}$ such that the initial slope and the saturation value equal unity. Also shown are the limits $b/a=0$ [thin strip, $m/m_{sat}=\tanh h$, Eq. (14)] and $b/a=\infty$ (long slab, $m/m_{sat}=h-h^2/4$ for $h\leq 2$, $m/m_{sat}=1$ for $h>2$). Bottom: deviation from the limit $b=0$, $m/m_{sat}-\tanh h$.

Comparing Figs. 8–10 to Figs. 7, 13, and 14 of Ref. 1 (which were computed with the same grid size) one notes that the magnetic field distributions at the upper surfaces of cylinders in axial H_a and of bars in perpendicular H_a are almost identical if the specimen cross section $2a\times 2b$ is the same. A small difference is that the deviation of the field profiles B_y on the flat surfaces $y=\pm b$ from that on the middle plane $y=0$ is larger for the disk than for the strip. This can be understood from the fact that the flat surface of a disk is surrounded by a current-free vacuum in both the x and z directions, while the strip surface sees the current-carrying strip in the z direction and thus behaves more like the bulk.

C. Virgin magnetization curves

Figures 11 and 12 show computed virgin magnetization curves of bars and cylinders with various aspect ratios b/a in the Bean limit ($n=101$). Plotted is the magnetic moment $M(H_a)$ in reduced units m/m_{sat} versus a reduced field $h=H_a m'(0)/m_{sat}$, such that the initial slopes and saturation values of all curves equal unity. Also shown are the limiting curves for parallel geometry $b/a\gg 1$, namely, $m/m_{sat}=h-h^2/4$ (long slab, $h\leq 2$) and $m/m_{sat}=h-h^2/3+h^3/27$ (long cylinder, $h\leq 3$) with $m/m_{sat}=1$ for $h\geq 2$ or $h\geq 3$, and perpendicular geometry in the thin-film limit $b/a\ll 1$, namely, $m/m_{sat}=\tanh h$ (thin strip) and $m/m_{sat}=f_d(h)$ (thin circular disk) with

$$f_d(h)=\frac{2}{\pi}\left(\cos^{-1}\frac{1}{\cosh(\pi h/4)}+\frac{\sinh(|\pi h/4|)}{\cosh^2(\pi h/4)}\right); \quad (36)$$

cf. Eqs. (4)–(6) and (11)–(13). The Bean magnetization curves for thin strips and disks in reduced units almost coincide, $0\leq f_d(h)-\tanh h<0.011$, with maximum deviation at $h=1.37$. The lower plots in Figs. 11 and 12 show the deviation of the computed reduced magnetic moment from the thin-film limit. Note that this deviation is small and nonmonotonic as a function of b/a. The deviation is largest for $h\approx 1$ and $b/a\approx 0.6$.

The saturated magnetic moment $m_{sat}=m(H_a\to\infty)$ and initial slope $m'(0)$ of the magnetization curves in real units are given by the following expressions. In the Bean limit ($n\to\infty$) one has, for long bars of length l, $m_{sat}=-2J_c a^2 bl$ and, for cylinders of length $2b$, $m_{sat}=-(2\pi/3)J_c a^3 b$; cf. Eq. (6). For finite creep exponents $n<\infty$ in the current-voltage law $E=E_c(J/J_c)^n$, the saturation value of m depends on the ramp rate $\dot{B}_a$ of the applied field and is reached exponentially in time if $\dot{B}_a=\text{const.}$[1] For bars and strips with length l one has[1]

$$m_{sat}=-2J_c a^2 bl\left(\frac{\dot{B}_a a}{E_c}\right)^{1/n}\frac{2n}{2n+1}. \quad (37)$$

For cylinders and disks the result[25,51]

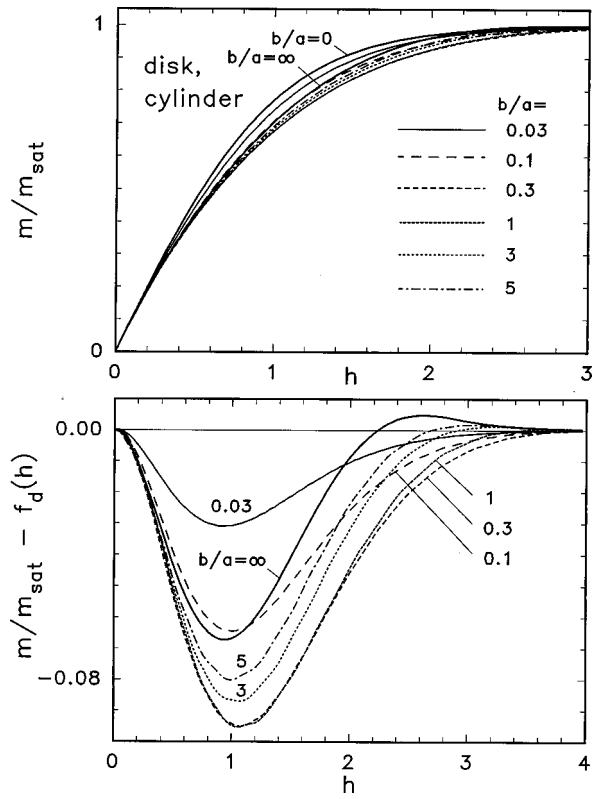

FIG. 12. Top: as in Fig. 11, but for disks and cylinders with various aspect ratios b/a in increasing axial field. The reduced units and limits for $b/a=0$ [thin disk, $m/m_{\rm sat}=f_d(h)$ and $b/a=\infty$ (long cylinder), $m/m_{\rm sat}=h-h^2/3+h^3/27$ for $h\leqslant 3$, $m/m_{\rm sat}=1$ for $h>3$] follow from Eqs. (4)–(6) and (11)–(13). Bottom: deviation from the limit $b=0$, $m/m_{\rm sat}-f_d(h)$.

$$m_{\rm sat}=-\frac{2\pi}{3}J_c a^3 b\left(\frac{\dot B_a a}{2E_c}\right)^{1/n}\frac{3n}{3n+1} \tag{38}$$

is obtained by inserting in Eq. (3) the electric field $E(r)$ and current density $J(r)=J_c(E/E_c)^{1/n}$ of the saturated state,

$$E_{\rm sat}(r)=\frac{r}{2}\dot B_a\,, \tag{39}$$

$$J_{\rm sat}(r)=J_c\left(\frac{r}{a}\right)^{1/n}\left(\frac{\dot B_a a}{2E_c}\right)^{1/n}. \tag{40}$$

The initial slope $m'(0)$ is computed from the surface-screening current $J_{\rm scr}(\mathbf{r})$, Eq. (26). With Eq. (3) this yields

$$m'(0)=-\pi\int_0^a dx\int_0^b dy\int_0^a dx'\int_0^b dy'\; r^2 Q^{-1}(\mathbf{r},\mathbf{r}')r'. \tag{41}$$

On an appropriate grid with positions $\mathbf{r}_i$ and weights w_i [cf. Eq. (29) and the Appendix] one computes this as

$$m'(0)=-\pi\sum_{ij}\; w_i r_i^2 (Q_{ij}w_j)^{-1} r_j\,. \tag{42}$$

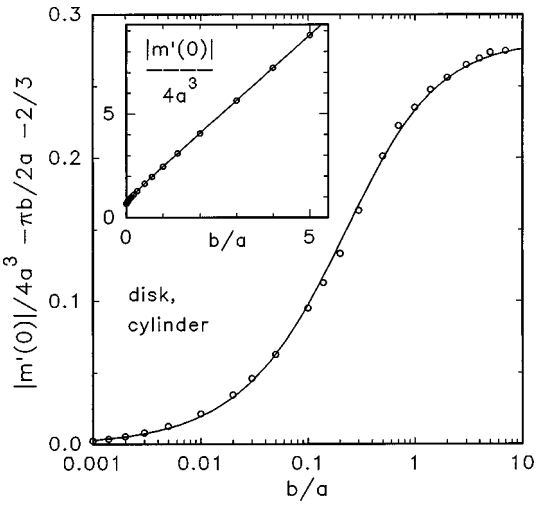

FIG. 13. The initial slope $|m'(0)|$ of the virgin magnetization curve $m(H_a)$ of disks and cylinders in an axial field H_a, equal to the ideal diamagnetic moment $m_{\rm scr}(H_a)=H_a m'(0)$, as a function of the aspect ratio b/a. The dots are computed using Eq. (42) and the lines show the fit formula (43). The inset shows the full $|m'(0)|$. The main plot gives the small difference $|m'(0)|-\pi b/2a-3/2$, which vanishes in the thin-disk limit $b\ll a$ and takes the value 0.42 in the limit $b\gg a$.

To a very good approximation with relative error $<1\%$ one may write the resulting initial slope (or ideal diamagnetic moment) of cylinders with radius a and length $2b$ in an axial field as

$$\frac{-m'(0)}{4a^3}=\frac{\pi b}{2a}+\frac{2}{3}+\frac{1}{3}\tanh\left[1.27\frac{b}{a}\ln\left(1+\frac{a}{b}\right)\right]. \tag{43}$$

This formula has the correct limits $m'(0)=-8a^3/3$ for $b\ll a$ and $m'(0)=-2\pi a^2 b$ for $b\ll a$; cf. Eqs. (12) and (5). The last term in Eq. (43) is a small fitted correction. The computed slope $m'(0)$ for cylinders is plotted in Fig. 13 together with the fit (43). The corresponding slope for bars [given by Fig. 15 and Eq. (77) in Ref. 1] in principle can be calculated analytically by conformal mapping, but for the cylinder this method does not work.

D. Magnetization loops

Figure 14 shows hysteresis loops of the magnetic moment $m(H_a)$ of a round cylinder with aspect ratio $b/a=1$ (square cross section) for three creep exponents $n=51$, 11, and 5. The amplitudes $B_0=\mu_0 H_0$ of the cycled applied field are $H_0/H_p=1.5$, 1, and 0.5, where H_p is the field (19) of full penetration. For cylinders with $b/a=1$ one has $H_p=0.8814J_c a$. In the upper plot the applied field was increased and decreased zigzaglike, i.e., at a constant ramp rate $\dot H_a(t)=(2\omega/\pi)H_0\,\mathrm{sgn}(\cos\omega t)$, and in the lower plot sinusoidally, $H_a(t)=H_0\sin\omega t$, $\dot H_a(t)=H_0\cos\omega t$. In both plots $\omega=1$ was chosen, which with our reduced units $a=J_c=E_c=\mu_0=1$ means $\omega=E_c/(\mu_0 J_c a^2)$ in physical units. As stated in Sec. II E, the choice of this frequency is irrelevant since any other frequency leads to exactly the same magnetization loops if the unit of the magnetic field is changed appropriately. In all loops in Figs. 14–17 the time ranges

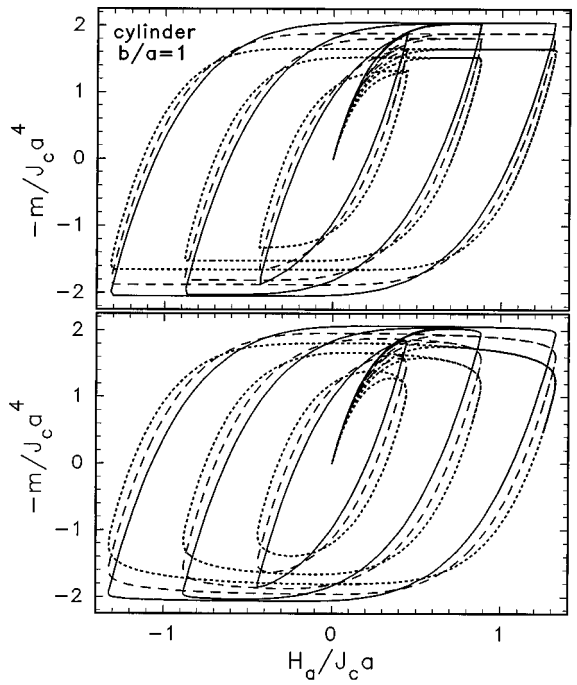

FIG. 14. Magnetization loops $m(H_a)$ of a cylinder with aspect ratio $b/a=1$ for creep exponents $n=51$ (bold lines), $n=11$ (dashed lines), and $n=5$ (dotted lines) at amplitudes of the cycled applied field $H_0/H_p=1.5$, 1, and 0.5, where $H_p=0.8814J_c a$ is the field of full penetration, Eq. (19). Top: zigzag applied field with piecewise constant ramp rate $\dot{H}_a(t)=(2\omega/\pi)H_0\mathrm{sgn}(\cos\omega t)$. Bottom: sinusoidal $H_a(t)=H_0\sin\omega t$ with same frequency $\omega=E_c/(\mu_0 J_c a^2)=1$ in reduced units $a=J_c=E_c=\mu_0=1$. The plotted time interval is $t=0,\ldots,2.6\pi$, which means 1.3 cycles including the virgin curves.

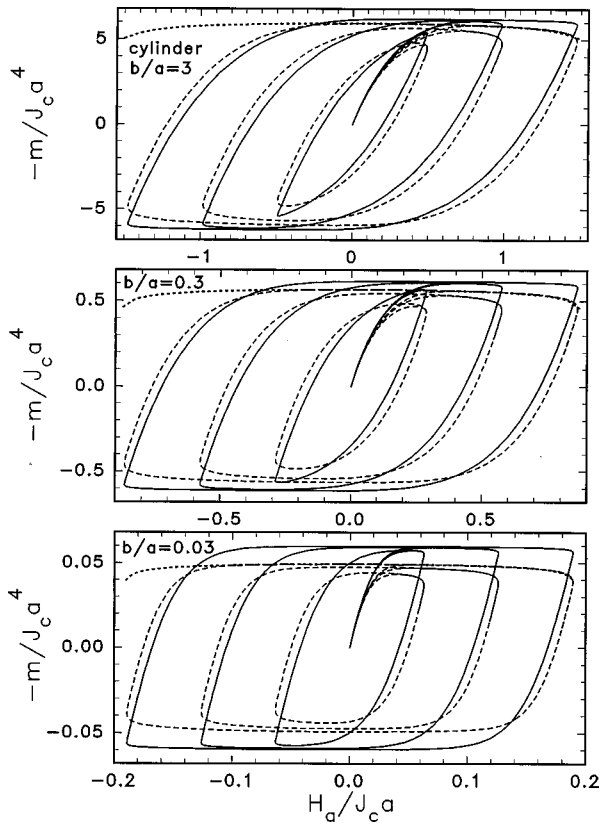

FIG. 15. Magnetization loops $m(H_a)$ of cylinders with $b/a=3$ (long cylinder, top), 0.3 (short cylinder, middle), and 0.03 (thin disk, bottom) for creep exponents $n=51$ (bold lines) and $n=11$ (dashed lines) in a sinusoidal field $H_a(t)=H_0\sin\omega t$ at amplitudes $H_0/H_p=1.5$, 1, and 0.5 (here $H_p/J_c a=0.9824$, 0.5757, 0.1260) and frequency $\omega=1$ like in Fig. 14. The dotted lines give Eq. (44), which describes the upper and lower branches of $m(H_a)$.

from $t=0$ to $t=2.6\pi$, corresponding to 1.3 cycles including the virgin curves ($0\leqslant t\leqslant\pi/2$, 1/4 cycle).

Remarkably, the stationary situation is reached (i.e., the memory about the magnetic history is lost) already after 1/4 cycle or even ealier at large amplitudes $H_0>H_p$. This can be seen from the fact that the loop precisely closes after one complete cycle at $t=2.5\pi$. So for $2.5<t/\pi<2.6$ the depicted magnetization curves show two closely coinciding lines, and all loops exhibit inversion symmetry. The rapid loss of magnetic memory is due to the nonlinearity of the current-voltage law used, $E(J)\propto J^n$, with $n\geqslant 5$ in these plots. In the Ohmic case $n=1$, the stationary hysteresis loop is reached exponentially in time, but for $n>1$ it is reached faster.

Note that in Fig. 14 the zigzag and sinusoidal applied fields yield almost the same hysteresis loop if n is large, in accordance with the prediction of the critical state model. A small difference is that for $|\dot{H}_a|=\mathrm{const}$, the saturation $m\rightarrow m_{\mathrm{sat}}$ is reached exponentially in time [Eq. (42) of Ref. 1], while for $H_a=H_0\sin\omega t$ the upper and lower branches of the magnetization loops are slightly curved, closely fitting the prediction[25]

$$m(H_a)=\pm m_{\mathrm{sat}}(1-H_a^2/H_0^2)^{1/(2n)}, \tag{44}$$

where m_{sat} is given by Eq. (38) [or Eq. (37) for the bar] with $\dot{B}_a=\omega\mu_0 H_0$ inserted. As is shown in Fig. 15, the theoretical curve (44) closely fits the upper and lower branches of the computed magnetization loops. This close coincidence proves that the slight decrease of the magnetization loops after the maximum was reached at $H_a=0$ is not a direct consequence of flux creep. In fact this decrease is absent for zigzag $H_a(t)$ but occurs with sinusoidal $H_a(t)$, where it reflects the gradual *decrease of the ramp rate* $\dot{H}_a(t)$ after $H_a(t)$ has passed through zero.[52] Therefore, also $E\approx(r/2)\dot{B}_a$ and $J\propto E^{1/n}$ decrease; cf. Eqs. (39) and (40).

Magnetization loops for cylinders and disks with aspect ratios $b/a=3$, 0.3, and 0.03 are depicted in Fig. 15 for creep exponents $n=51$ and $n=11$ in a sinusoidal $H_a(t)$ at amplitudes $H_0/H_p=1.5$, 1, and 0.5 ($H_p/J_c a=0.9824$, 0.5757, 0.1260) and frequency $\omega=1$ like in Fig. 14. Note that all these loops are very similar. They are also similar to the corresponding loops of bars. For comparison, Fig. 16 shows magnetization loops for a bar with a square cross section ($b/a=1$, like Fig. 14) in a perpendicular applied field $H_a(t)=H_0\sin\omega t$ at four amplitudes $H_0/H_p=2$, 1.5, 1, and 0.5 ($H_p=0.7206J_c a$ for this bar) and $\omega=E_c/(\mu_0 J_c a^2)=1$ for creep exponents $n=5$, 11, and 51.

E. Field-dependent $J_c(B)$

Also shown in Fig. 16 is one example for a field-dependent critical current density $J_c(B)=J_{c0}/(1+|B|/B_1)$ (Kim model) entering the law $E(J)=E_c[J/J_c(B)]^n$. Here

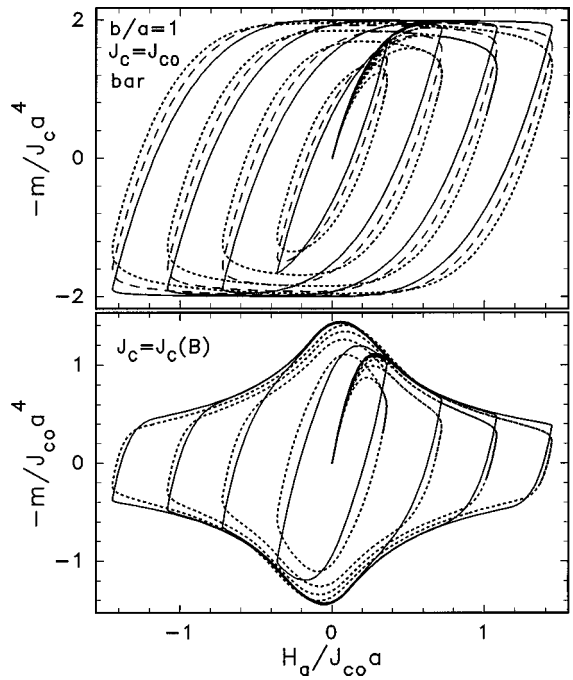

FIG. 16. Magnetization loops of a long bar with square cross section $b/a=1$, as the cylinder in Fig. 14, in a perpendicular applied field $H_a(t)=H_0\sin\omega t$ at four amplitudes $H_0/H_p=2$, 1.5, 1, and 0.5 ($H_p=0.7206J_c a$ for this bar) and $\omega=E_c/(\mu_0 J_c a^2)=1$ for creep exponents $n=5$ (solid line), $n=11$ (dashed lines), and $n=51$ (dotted lines). Top: constant critical current density $J_c=J_{c0}$ (Bean model). Bottom: field-dependent $J_c(B)=J_{c0}/(1+|B|/B_1)$ (Kim model) with $B_1/\mu_0=0.3603J_{c0}a=\frac{1}{2}H_p$ inserted into $E(J)=E_c[J/J_c(B)]^n$. Here $\omega=E_c/(\mu_0 J_{c0}a^2)=1$ in units $a=J_{c0}=E_c=\mu_0=1$. The loop for $n=11$, falling between the two depicted curves, is omitted for clarity.

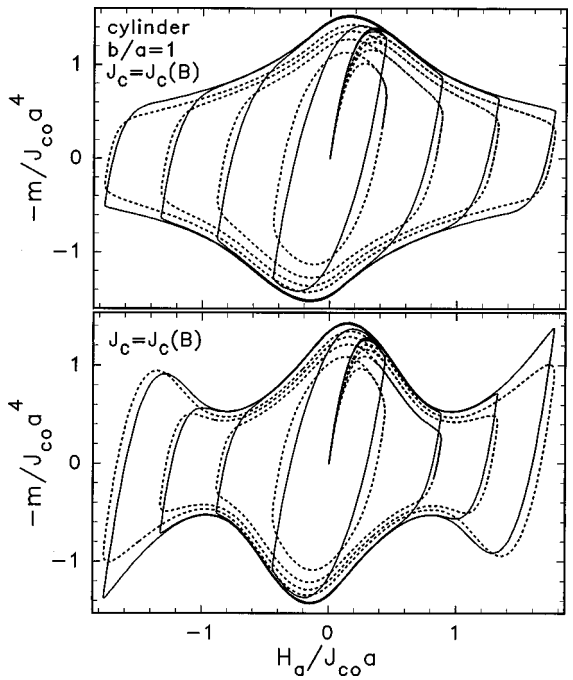

FIG. 17. Magnetization loops of cylinders with field-dependent critical current density $J_c(B)$ for $b/a=1$, creep exponents $n=51$ (bold lines) and $n=5$ (dotted lines), at amplitudes $H_0/H_p=2$, 1.5, 1, and 0.5 of the applied field $H_a=H_0\sin\omega t$($H_p=0.8814J_c a$, $\omega=1$ as in Figs. 14–16). Top: Kim model $J_c(B)=J_{c0}/(1+3\beta)$ with $\beta(\mathbf{r})=|B|/(\mu_0 H_p)$. Bottom: nonmonotonic model $J_c(B)=J_{c0}(1-3\beta+3\beta^2)$. Both $J_c(B)$ have the same initial slope, but at large H_a the lower plot exhibits a ''fishtail effect.''

we chose $B_1/\mu_0=H_p/2=0.3603J_{c0}a$ (for this bar) and $\omega=E_c/(\mu_0 J_{c0}a^2)=1$ in units $a=J_{c0}=E_c=\mu_0=1$. For such figures the required local induction $\mathbf{B}(\mathbf{r})$ is most conveniently computed from the current density $\mathbf{J}(\mathbf{r})$ using the Biot-Savart law and the specimen symmetry. This integration is much more accurate than taking the numerical derivative of the vector potential $\mathbf{A}(\mathbf{r})$, and it works even for very small numbers of grid planes, N_x or N_y (as small as 3), reproducing the field-free central zone with an accuracy of up to 10^{-12}. The integral kernel relating $\mathbf{B}(\mathbf{r})=\nabla\times\mathbf{A}$ to $J_\varphi(\mathbf{r}')$ follows from Eq. (20) as $-\mu_0\nabla_{\mathbf{r}}\times Q_{\rm cyl}(\mathbf{r},\mathbf{r}')$.

Figure 17 shows two examples for magnetization loops of cylinders with field-dependent $J_c(B)$. As in Figs. 14 and 16, the aspect ratio was $b/a=1$, creep exponents $n=51$ and $n=5$ are shown, and a field $H_a=H_0\sin\omega t$ was applied. For the upper plot we chose the Kim model $J_c(B)=J_{c0}/(1+3\beta)$ with $\beta(\mathbf{r})=|\mathbf{B}(\mathbf{r})|/(\mu_0 H_p)$ (here $H_p=0.8814J_c a$), which means a monotonically decreasing $J_c(B)$. In the lower plot, to simulate the so-called fishtail effect (or peak effect, butterfly effect) we chose a nonmonotonic critical current density $J_c(B)=J_{c0}(1-3\beta+3\beta^2)$, which has the same initial slope as the Kim model used in the upper plot. The virgin curves in both plots of Fig. 17 thus look very similar. But with increasing H_a the magnetization in the lower plot goes through a minimum that reflects the minimum in $J_c(B)$. Note that J_c depends on the *local* flux density B, which in general is different from the applied field $B_a=\mu_0 H_a$. Only at large applied fields $H_a\gg H_p$ does the relative variation of $B(\mathbf{r})$ become small compared to the average B, which then approximately equals B_a; cf. Figs. 9 and 10.

Whereas for constant J_c the current density in the penetrated regions in the cylinder saturates to $\pm J_c$, the B-dependent $J_c(B)$ causes a nonconstant J in these regions. Examples for the resulting current profiles $J(r,y)$ are shown in Fig. 18 for the same cylinder as in the upper plot of Fig. 17 [$b/a=1$, $J_c(B)=J_{c0}/(1+3|B|/\mu_0 H_p)$], at one amplitude $H_0=H_p=0.8814J_c a$ and creep exponent $n=21$. For comparison, in Fig. 19 the profiles are shown for the same cylinder but with constant $J_c=J_{c0}$. In both plots the profiles are depicted at fields $H_a/(J_c a)=0.36$, 0.54, 0.88, and 0.60, corresponding to times $\omega t=0.42$, 0.66, 1.60, and 2.39. For these plots only $N_r\times N_y=11\times 11$ equidistant grid points were used, yielding still smooth profiles and smooth magnetization loops. In the upper plots of Figs. 18 and 19 (virgin curve, $H_a<H_p$) the field- and current-free central zone is clearly seen. In Fig. 18 the current profiles of the virgin curve have sharp ridges, which are not easily understood, while in the saturated state (third plot from above, $H_a=H_p$) the monotonically decreasing $J(\mathbf{r})$ is due to the nearly constant slope of the flux density B entering $J_c(B)$; cf. Figs. 8–10. In the lowest plot (decreasing $H_a<H_p$) the penetration of currents of opposite orientation is obvious. In Fig. 19 the slight curvature of the current profiles (in spite of constant J_c) is caused by the finite creep exponent $n=21$; for $n\geqslant 51$ these plateaus look perfectly flat; cf. Figs. 4 and 5 of Ref. 1.

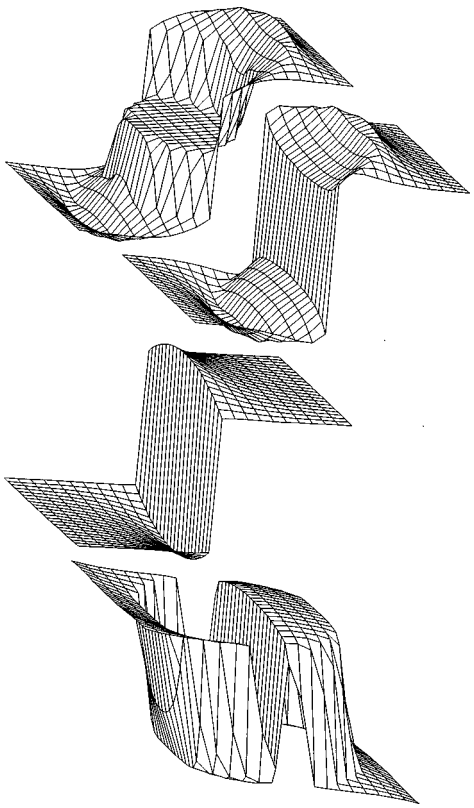

FIG. 18. Current profiles $J(r,y)$ for the same cylinder with field-dependent $J_c(B)$ as in Fig. 17 top, namely, $b/a=1$ and $J_c(B)=J_{c0}/(1+3|B|/\mu_0 H_p)$, at amplitude $H_0=H_p=0.8814J_c a$ of $H_a=H_0\sin\omega t$ with creep exponent $n=21$. From top to bottom the applied fields are $H_a/(J_c a)=0.36$, 0.54, 0.88, and 0.60, corresponding to times $\omega t=0.42$, 0.66, 1.60, and 2.39. The used grid has only $N_r\times N_y=11\times 11$ points.

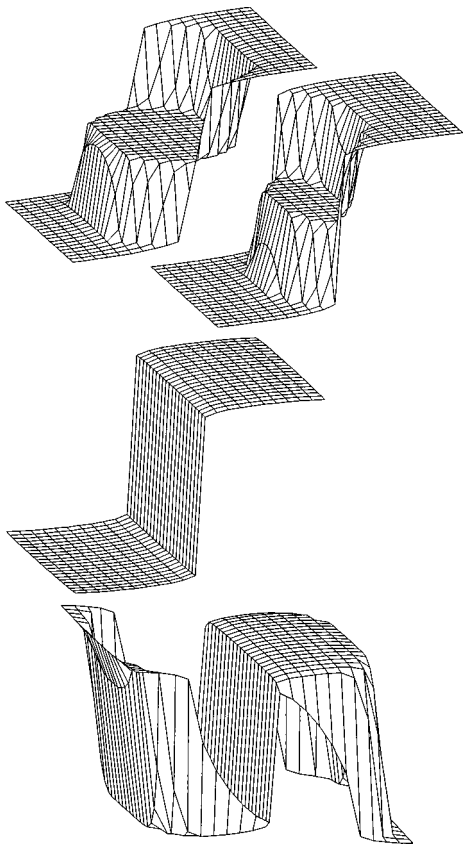

FIG. 19. Current profiles as in Fig. 18 but for constant J_c. Otherwise, the same cylinder and same amplitudes are shown.

V. CONCLUDING REMARKS

The magnetic field and current profiles and the magnetic moment of finite cylinders in an axial magnetic field are calculated from first principles. The presented method is very effective and elegant, since it directly calculates the current density inside the cylinder and does not require any approximation or cutoff of the magnetic field in the infinite space outside the cylinder. This novel method avoids any numerical differentiation but uses only integrals over the specimen cross section. It is fast and stable and works very well even on a PC. Our method applies to conductors and superconductors with axial symmetry, but otherwise with an arbitrary cross section like cylinders of finite length, thin and thick disks, cones, spheres, and rotational ellipsoids. The specimen may even be inhomogeneous and anisotropic[13] as long as axial symmetry pertains.

In our calculations the material is assumed to be nonmagnetic ($B=\mu_0 H$) but conducting, with either a nonlinear resistivity or with a linear complex and frequency-dependent resistivity. Both types of $E(J)$ laws successfully model type-II superconductors with pinning and thermally activated depinning of Abrikosov vortices in different situations. For the nonlinear case a power law $E(J)=E_c[J/J_c(B)]^{n(B)}$ was assumed, but for any other $E(J)$ curve this method works as well. For the linear case the results are even more general and will be presented in part II (Ref. 2) in the form of complex ac susceptibilities which depend only on the geometry (here, on the aspect ratio b/a) but otherwise apply to any linear and frequency-dependent resistivity.[53]

While the considered $E(J)$ dependence may be quite general, the assumption $\mathbf{B}=\mu_0\mathbf{H}$ in our theory (which disregards the lower critical field B_{c1}) cannot be relaxed so far. The extension to arbitrary reversible magnetization $B(H)$ with finite B_{c1} is under way. Therefore, the presented method so far does not allow one to compute geometric surface barriers,[19,54] though it may simulate surface (or edge) barriers by using an inhomogeneous critical current density $J_c(\mathbf{r})$.[55] It also cannot describe the ''current string'' discussed and observed by Indenbom *et al.*,[56] which occurs in the center of a superconductor strip with finite thickness due to the abrupt jump of $B(H)$ at the penetrating flux front. Both interesting phenomena will automatically result from an extension of our calculations to arbitrary $B(H)$. For recent progress in this direction and explicit calculations of the edge barrier for flux penetration into superconductors with a rectangular cross section see Refs. 57–59. See also the older analytical calculations[60] of the edge barrier for flux penetration into type-I superconductors.

If one is only interested in the Bean limit, one may compute the magnetization curve of short cylinders by Prigozhin's elegant variational method[4] or by static finite element methods,[61] which in principle work also in fully three-dimensional geometries.[62] Part II (Ref. 2) of this paper deals with the linear and nonlinear susceptibilities of finite cylinders calculated by the present method.

ACKNOWLEDGMENTS

I acknowledge useful discussions with L. Prigozhin, M. V. Indenbom, A. Gurevich, A. Forkl, Ch. Jooss, R. Warthmann, J. Gilchrist, J. R. Clem, and R. P. Huebener. This work was supported by the German-Israeli Foundation for Research and Development, Grant No. I-300-101.07/93.

APPENDIX A: THE INTEGRAL KERNEL

The integral kernels $Q(\mathbf{r},\mathbf{r}')$ required above and in Ref. 1 are Green's functions of the Laplace equation in particular geometries. In general, the equation for the vector potential $\mathbf{A}(\mathbf{r})$

$$\mu_0\mathbf{J}(\mathbf{r})=-\nabla^2\mathbf{A}(\mathbf{r}), \tag{A1}$$

is solved by

$$\mathbf{A}(\mathbf{r})=-\mu_0\int_V dV'\ Q(\mathbf{r},\mathbf{r}')\ \mathbf{J}(\mathbf{r})\ , \tag{A2}$$

where the integral $\int_V dV$ is over the volume in which the current density $\mathbf{J}(\mathbf{r})$ flows. In the three-dimensional infinite space, $Q(\mathbf{r},\mathbf{r}')=1/(4\pi|\mathbf{r}-\mathbf{r}'|)$ is well known. For a bar with infinite extension along $\hat{\mathbf{z}}$ and with an arbitrarily shaped cross section in a perpendicular field, $\mathbf{A}$ and $\mathbf{J}$ are along $\hat{\mathbf{z}}$ and integration over z' yields

$$Q_{\rm bar}(\mathbf{r},\mathbf{r}')=\frac{1}{2\pi}\ln|\mathbf{r}-\mathbf{r}'|, \tag{A3}$$

with $\mathbf{r}=(x,y)$. For cylinders in an axial field, $\mathbf{A}$ and $\mathbf{J}$ are along $\hat{\varphi}$ and integration over φ yields

$$Q_{\rm cyl}(\mathbf{r},\mathbf{r}')=f(r,r',y-y'), \tag{A4}$$

with $f(r,r',y-y')$ given by Eq. (26) and $\mathbf{r}=(r,y)$, $r=\sqrt{x^2+z^2}$. The kernel (A4) is more general than Eq. (25), which applies only if the axially symmetric specimen has an additional symmetry plane $y=0$. In both bar and cylinder geometries one may write

$$\mathbf{A}(\mathbf{r})=-\mu_0\int_S d^2r'\ Q_2(\mathbf{r},\mathbf{r}')\ \mathbf{J}(\mathbf{r}')\ , \tag{A5}$$

where $Q_2(\mathbf{r},\mathbf{r}')$ means $Q_{\rm bar}$ or $Q_{\rm cyl}$. The integral (A5) may be evaluated numerically by introducing a 2D grid of N points $\mathbf{r}_i$ with weights (grid cell areas) w_i. This grid has to span the cross section S of the bar or cylinder (or one-half or one-quarter of it, depending on the specimen symmetry) and may be chosen equidistant or nonequidistant, preferably such that the grid is denser near the specimen surface.

A possible equidistant grid of $N=N_rN_y$ points $\mathbf{r}_i=(r_i,y_i)$ with constant weights $w_i=ab/N$ is $r_i=r_k=(k-\frac{1}{2})a/N_r(k=1,\ldots,N_r)$, $y_i=y_l=(l-\frac{1}{2})b/N_y(l=1,\ldots,N_y)$. A possible nonequidistant grid $\mathbf{r}_i=(r_i,y_i)$ is obtained by the substitutions $r=r(u)=\frac{1}{2}(3u-u^3)a$, $y=y(v)=\frac{1}{2}(3v-v^3)b$, and then tabulating $u=0,\ldots,1$ and $v=0,\ldots,1$ on equidistant grids $u_k=(k-\frac{1}{2})/N_r(k=1,\ldots,N_r)$ and $v_l=(l-\frac{1}{2})/N_y(l=1,\ldots,N_y)$; this yields a 2D grid of $N=N_r\times N_y$ points with weights $w_i=w_rw_y$, $w_r=dr_k/dk=\frac{3}{2}(1-u_k^2)a/N_r$, and $w_y=dy_l/dl=\frac{3}{2}(1-v_l^2)b/N_y$, which vanish at the cylinder boundaries $r=a$ and $y=b$.

With an appropriate grid one has, for any sufficiently smooth function $f(\mathbf{r})$ defined in the area S,

$$\int_S d^2r\ f(\mathbf{r})\approx\sum_i\ f(\mathbf{r}_i)w_i\,. \tag{A6}$$

In particular, Eq. (A5) is approximated by

$$A_i=-\mu_0\sum_j\ Q_{ij}w_jJ_j\,, \tag{A7}$$

with $A_i=A(\mathbf{r}_i)$, $J_i=J(\mathbf{r}_i)$, and $Q_{ij}=Q(\mathbf{r}_i,\mathbf{r}_j)$. This matrix equation is easily inverted to give

$$\mu_0J_i=-\sum_j\ (Q_{ij}w_j)^{-1}A_j\,, \tag{A8}$$

where $(Q_{ij}w_j)^{-1}$ is the reciprocal matrix of $Q_{ij}w_j$ (no summation over j).

The kernels $Q_{\rm bar}$, Eq. (A3), and $Q_{\rm cyl}$, Eq. (A4), have a logarithmic infinity when $\mathbf{r}\to\mathbf{r}'$. This means that the diagonal elements of the matrix Q_{ij} formally are infinite and thus have to be defined separately. The optimum choice of these diagonal terms is an intricate problem which is not yet solved completely. For the 1D problems of thin strips and thin disks with integral kernel $Q(x,x')$, maximum accuracy is achieved by choosing the diagonal terms $Q_{ii}=Q(x_i,x_i)$ such that an infinitely extended superconducting thin film ideally screens the magnetic field of a coil placed on one side of the film.[33] This definition is identical to choosing Q_{ii} such that

$$\sum_j\ Q_{ij}=\int_S dx'\ Q(x_i,x') \tag{A9}$$

is exactly satisfied.[35,36] This choice replaces in the 1D kernel the diverging logarithm $\ln|x_i-x_j|$ at $i=j$ for the strip by[35] $\ln(w_i/2\pi)$, where w_i is the (in general nonconstant) grid spacing or weight, and for the disk by[36] $\ln(0.923\,63w_i/2\pi)$, where[33] $0.923\,63=\exp(2)/8$.

For the 2D problems of bars and cylinders, such a choice of Q_{ii} did not work well as yet, possibly due to limited numerical accuracy. However, a different choice of the Q_{ii} works satisfactorily, namely, equating $Q_{ii}w_i$ to the integral of $Q(\mathbf{r}_i,\mathbf{r}')$ over the grid cell area w_i centered at $\mathbf{r}'=\mathbf{r}_i$. For rectangular grid cells this means that when $i=j$, one then replaces in both Eqs. (A3) and (A4) the term $(y_i-y_j)^2$ by a small area ϵ_i^2 given by

$$\epsilon_i^2=\exp\left[\ln(u^2+v^2)-3+\frac{u}{v}\mathrm{atan}\frac{v}{u}+\frac{v}{u}\mathrm{atan}\frac{u}{v}\right], \tag{A10}$$

where $u=dx/2$ and $v=dy/2$ are the half widths of the ith rectangular grid cell with area $w_i=4uv=dx\,dy$. Here I have used the formula

$$f(u,v)=\int_0^u dx\int_0^v dy\ \ln(x^2+y^2)=uv\ln(u^2+v^2)-3uv$$
$$+u^2\mathrm{atan}\frac{v}{u}+v^2\mathrm{atan}\frac{u}{v}. \qquad \text{(A11)}$$

In particular, for square-shaped grid cells of width $2u=2v=dx=dy$ one has

$$\epsilon_i^2=\exp(\ln 2u^2-3+\pi/2)=0.12\ dx\ dy. \qquad \text{(A12)}$$

Formula (A10) is exact for equidistant rectangular grid cells, but it is also a good approximation for grid cells of varying size. In the limit $b\to 0$, $N_y=1$, these diagonal terms nearly reproduce those which follow from condition (A9).

The choice (A10) appears to yield maximum accuracy when one calculates the linear ac susceptibilities of bars or cylinders, Sec. IV E. However, in the calculation of flux penetration, the choice (A10) for the Q_{ij} leads to large unphysical spatial oscillations of the profiles of the current density near the flux front. This artifact is suppressed by choosing larger diagonal terms, e.g., by dividing ϵ_i^2, Eq. (A10), by a factor of up to 8. This finding partly explains why the heuristic choice $\epsilon_i^2=0.015\ dx\ dy$ works so well.

A more rigorous choice of the integral kernels, which automatically yields finite diagonal elements, is the method of finite elements.[4] But so far the diagonal elements obtained in this way proved to be too small and led to artificially oscillating current profiles. Here again the enhancing of the diagonal terms of the matrix ''by hand'' suppresses these oscillations.

[1] E. H. Brandt, Phys. Rev. B **54**, 4246 (1996).
[2] E. H. Brandt, following paper, Phys. Rev. B **58**, 6523 (1998).
[3] C. P. Bean, Phys. Rev. Lett. **8**, 250 (1962); Rev. Mod. Phys. **36**, 31 (1964).
[4] L. Prigozhin, Eur. J. Appl. Math. **7**, 237 (1996); Phys. Rev. E **49**, 1161 (1994); Free Boundary Problems Newsletter **10**, 2 (1996); J. Comput. Phys. **129**, 190 (1996); J. Comput. Phys. (to be published); IEEE Trans. Appl. Supercond. **7**, 3866 (1997).
[5] Th. Schuster, M. V. Indenbom, M. R. Koblischka, H. Kuhn, and H. Kronmüller, Phys. Rev. B **49**, 3443 (1994).
[6] P. Brüll, D. Kirchgässner, and P. Leiderer, Physica C **182**, 339 (1991); R. L. Prozorov, A. A. Polyanskii, V. I. Nikitenko, I. V. Grekhov, L. A. Delimova, and I. A. Liniichuk, Sverkhprovodimost' **6**, 1714 (1993) [Supercond., Phys. Chem. Technol. **6**, 563 (1993)]; A. A. Polyanskii, A. Gurevich, A. E. Pashitski, N. F. Heinig, R. D. Redwing, J. E. Nordman, and D. C. Larbalestier, Phys. Rev. B **53**, 8687 (1996).
[7] H. Theuss, A. Forkl, and H. Kronmüller, Physica C **190**, 345 (1992); Th. Schuster, H. Kuhn, E. H. Brandt, M. Indenbom, M. R. Koblischka, and M. Konczykowski, Phys. Rev. B **50**, 16 684 (1994); Th. Schuster, H. Kuhn, and E. H. Brandt, *ibid.* **54**, 3514 (1996).
[8] P. D. Grant, M. W. Denhoff, W. Xing, P. Brown, S. Govorkov, J. C. Irwin, B. Heinrich, H. Zhou, A. A. Fife, and A. R. Cragg, Physica C **229**, 289 (1994); W. Xing, B. Heinrich, Hu Zhou, A. A. Fife, and A. R. Cragg, J. Appl. Phys. **76**, 4244 (1994).
[9] R. J. Wijngaarden, H. J. W. Spoelder, R. Surdeanu, and R. Griessen, Phys. Rev. B **54**, 6742 (1996).
[10] T. H. Johansen, M. Baziljevich, H. Bratsberg, Y. Galperin, P. E. Lindelof, Y. Shen, and P. Vase, Phys. Rev. B **54**, 16 264 (1996).
[11] A. E. Pashitskii, A. Gurevich, A. A. Polyanskii, D. C. Larbalestier, A. Goyal, E. D. Specht, D. M. Kroeger, J. A. DeLuca, and J. E. Taczyk, Science **275**, 367 (1997).
[12] Ch. Jooss, R. Warthmann, A. Forkl, H. Kronmüller, B. Leibold, and H.-U. Habermeier, Physica C **266**, 235 (1996); Ch. Jooss, R. Warthmann, A. Forkl, and H. Kronmüller, Physica C **299**, 215 (1998).
[13] Th. Schuster, H. Kuhn, E. H. Brandt, and S. Klaumünzer, Phys. Rev. B **56**, 3413 (1997).
[14] E. H. Brandt, Phys. Rev. Lett. **74**, 3025 (1995); Phys. Rev. B **52**, 15 442 (1995).
[15] Th. Schuster, H. Kuhn, E. H. Brandt, M. V. Indenbom, M. Kläser, G. Müller-Vogt, H.-U. Habermeier, H. Kronmüller, and A. Forkl, Phys. Rev. B **52**, 10 375 (1995).
[16] L. Prigozhin, IEEE Trans. Appl. Supercond. **AS-7**, 3866 (1997).
[17] P. N. Mikheenko and Yu. E. Kuzovlev, Physica C **204**, 229 (1993).
[18] E. H. Brandt, M. Indenbom, and A. Forkl, Europhys. Lett. **22**, 735 (1993).
[19] E. H. Brandt, Rep. Prog. Phys. **58**, 1465 (1995).
[20] W. T. Norris, J. Phys. D **3**, 489 (1970).
[21] E. H. Brandt and M. Indenbom, Phys. Rev. B **48**, 12 893 (1993).
[22] E. Zeldov, J. R. Clem, M. McElfresh, and M. Darwin, Phys. Rev. B **49**, 9802 (1994).
[23] Y. Yang, T. Hughes, C. Beduz, D. M. Spiller, R. G. Scurlock, and W. T. Norris, Physica C **256**, 378 (1996).
[24] E. H. Brandt, Physica C **235-240**, 2939 (1994).
[25] E. H. Brandt, Phys. Rev. B **55**, 14 513 (1997).
[26] F. Mrowka, M. Wurlitzer, P. Esquinazi, E. H. Brandt, M. Lorenz, and K. Zimmer, Appl. Phys. Lett. **70**, 898 (1997).
[27] Th. Herzog, H. A. Radovan, P. Ziemann, and E. H. Brandt, Phys. Rev. B **56**, 2871 (1997).
[28] A. M. Campbell and J. E. Evetts, Adv. Phys. **21**, 199 (1972).
[29] J. Zhu, J. Mester, J. Lockhart, and J. Turneaure, Physica C **212**, 216 (1993).
[30] R. W. Rollins and J. Silcox, Phys. Rev. **155**, 404 (1967); H. J. Fink, *ibid.* **161**, 417 (1967); D. de Klerk and C. A. M. van der Klein, J. Low Temp. Phys. **6**, 1 (1972).
[31] J. R. Clem and A. Sanchez, Phys. Rev. B **50**, 9355 (1994).
[32] A. Gurevich, Phys. Rev. B **46**, 3638 (1992).
[33] J. Gilchrist and E. H. Brandt, Phys. Rev. B **54**, 3530 (1996).
[34] A. Forkl, Phys. Scr. **T49**, 148 (1993).
[35] E. H. Brandt, Phys. Rev. B **49**, 9024 (1994); Phys. Rev. Lett. **71**, 2821 (1993).
[36] E. H. Brandt, Phys. Rev. B **50**, 4034 (1994).
[37] M. V. Feigel'man, V. B. Geshkenbein, A. I. Larkin, and V. M. Vinokur, Phys. Rev. Lett. **63**, 2303 (1989).
[38] T. Nattermann, Phys. Rev. Lett. **64**, 2454 (1990).
[39] D. S. Fisher, M. P. A. Fisher, and D. A. Huse, Phys. Rev. B **43**, 130 (1991).
[40] G. Blatter, M. V. Feigel'man, V. B. Geshkenbein, A. I. Larkin,

and V. M. Vinokur, Rev. Mod. Phys. **66**, 1125 (1994).
[41] P. H. Kes, J. Aarts, J. van der Berg, C. J. van der Beek, and J. A. Mydosh, Supercond. Sci. Technol. **1**, 242 (1989).
[42] J. Gilchrist and M. Konczykowski, Physica C **212**, 43 (1993).
[43] M. Ashkin, J. Appl. Phys. **50**, 7060 (1979).
[44] V. B. Zenkevich, V. V. Zheltov, and A. S. Romanyuk, Dokl. Akad. Nauk SSSR **251**, 339 (1980) [Sov. Phys. Dokl. **25**, 210 (1980)].
[45] R. Navarro and L. J. Campbell, Supercond. Sci. Technol. **5**, S200 (1992).
[46] K. L. Telschow and L. S. Koo, Phys. Rev. B **50**, 6923 (1994).
[47] E. H. Brandt, Phys. Rev. Lett. **76**, 4030 (1996).
[48] E. H. Brandt, Science **243**, 349 (1989); La Recherche (Paris) **224**, 998 (1990).
[49] M. V. Berry and A. K. Geim, Eur. J. Phys. **18**, 307 (1997).
[50] E. H. Brandt, Phys. World **10**, 23 (1997).
[51] Y. Mawatari, A. Sawa, H. Obara, M. Umeda, and H. Yamasaki, Appl. Phys. Lett. **70**, 2300 (1997).
[52] A. Gurevich (private communication).
[53] E. H. Brandt, Phys. Rev. B **50**, 13 833 (1994).
[54] E. Zeldov, A. I. Larkin, V. B. Geshkenbein, M. Konczykowski, D. Majer, B. Khaykovich, V. M. Vinokur, and H. Shtrikman, Phys. Rev. Lett. **73**, 1428 (1994); M. V. Indenbom and E. H. Brandt, *ibid.* **73**, 1731 (1994); E. Zeldov, A. I. Larkin, M. Konczykowski, M. Khaykovich, D. Majer, V. B. Geshkenbein, and V. M. Vinokur, Physica C **235-240**, 2761 (1994); I. L. Maksimov and A. A. Elistratov, Pis'ma Zh. Éksp. Teor. Fiz. **61**, 204 (1995) [JETP Lett. **61**, 208 (1995)]; N. Morozov, E. Zeldov, D. Majer, and B. Khaykovich, Phys. Rev. Lett. **76**, 138 (1996); C. J. van der Beek, M. V. Indenbom, G. D'Anna, and W. Benoit, Physica C **258**, 105 (1996).
[55] Th. Schuster, M. V. Indenbom, H. Kuhn, E. H. Brandt, and M. Konczykowski, Phys. Rev. Lett. **73**, 1424 (1994).
[56] M. V. Indenbom, Th. Schuster, H. Kuhn, H. Kronmüller, T. W. Li, and A. A. Menovsky, Phys. Rev. B **51**, 15 484 (1995).
[57] M. Benkraouda and J. R. Clem, Phys. Rev. B **53**, 5716 (1996).
[58] R. Labusch and T. B. Doyle, Physica C **290**, 143 (1997); T. B. Doyle, R. Labusch, and R. A. Doyle, *ibid.* **290**, 148 (1997).
[59] E. H. Brandt, Phys. Rev. Lett. (to be published).
[60] J. R. Clem, R. P. Huebener, and D. E. Gallus, J. Low Temp. Phys. **5**, 449 (1973); W. Buck, K.-P. Selig, and J. Parisi, *ibid.* **45**, 21 (1981); J. Provost, E. Paumier, and A. Fortini, J. Phys. F **4**, 439 (1974); A. Fortini, A. Haire, and E. Paumier, Phys. Rev. B **21**, 5065 (1980).
[61] J. Younas and J. H. P. Watson, Supercond. Sci. Technol. **10**, 187 (1997).
[62] A. Bossavit, IEEE Trans. Magn. **MAG-30**, 3363 (1994).